POSITION SENSORLESS IMPLEMENTATION FOR A LINEAR SWITCHED RELUCTANCE MACHINE

Brian MacCleery

A thesis submitted to the Faculty of the Virginia Polytechnic Institute and State University in partial fulfillment of the requirements for the degree of

MASTERS OF SCIENCE
in
Electrical Engineering

APPROVED:

Dr. Krishnan Ramu, Chair
Dr. Robert Hendricks
Dr. Charles Nunnally

July 17, 2000

Blacksburg, Virginia

Keywords: Switched reluctance, sensorless positioning, position estimator, LSRM, linear switched reluctance, magnetic propulsion

POSITION SENSORLESS IMPLEMENTATION FOR A LINEAR SWITCHED RELUCTANCE MACHINE

Brian MacCleery

Abstract

The development of an add-on sensorless position estimator for a 4.8 m Linear Switched Reluctance Machine (LSRM) with minimal modifications to the transducer-based controller is investigated for the first time in this study. LSRMs require position feedback for closed-loop control but present a low cost, high energy efficiency alternative for linear actuation due to their rugged construction and single-sided excitation. Mechanical position transducers mounted on the vehicle are expensive and can impact reliability. The use of a sensorless position estimator removes all electronics from the passive vehicle, resulting in considerable reductions in cost, maintenance, and mechanical complexity.

This study examines the use of an add-on processor and data acquisition system for sensorless position estimation. An approach exploiting the active phase windings is used to preserve the normal operation of the transducer-based DSP controller with the goal of limiting reductions in high performance features such as force ripple reduction and velocity control [3]. The estimator system is retrofit to the transducer-based DSP controller by mimicking the output of a mechanical position sensor by emulating a Quadrature encoder. The feasibility and design issues for an add-on or retrofit position estimator are investigated. Although sensorless schemes for rotary Switched Reluctance Machines (SRMs) have been studied in detail, the problem of sensorless implementations for LSRMs has not been addressed. Experimental validation of the proposed sensorless estimation scheme is attempted, but closed-loop operation is not achieved successfully due to air gap fluctuations. In depth analysis of the sources and propagation of error is presented.

Acknowledgments

The author wishes to acknowledge the contributions of a great number of faculty, students, and volunteers from various departments at Virginia Tech who contributed to the development of the prototype Linear Switched Reluctance Machine (LSRM) via the Personal Electric Rapid Transit Systems division of the Virginia Tech Virtual Corporation (VC-PERTS). In particular, he would like to thank Dr. Krishnan Ramu for his unfaltering confidence, trust, encouragement, and expert advice throughout the many happy years he had the good fortune of working for and learning from the great man known as R. Krishnan. He would also like to thank the other members of the Motion Control Systems Research Group (MCSRG) such as Phillip Vallance and the talented principal designers of the prototype such as Han-Kyung Bae, Byeong-Seok Lee, and Praveen Vijayraghavan. He would like to thank the undergraduate student members of the Fall 1999 Sensorless Positioning Team who volunteered to assist in the development and simulation of the sensorless algorithm. He would also like to thank National Instruments for their generous donation of the real-time computing engine and software used in this research via an undergraduate submission to the LabVIEW RT Applications Contest, and for their excellent technical support. Finally, he would like to thank Dr. Charles Nunnally, Dr. Leonard Ferrari, Dr. Robert Hendricks, Alice Quesenberry, and the entire Bradley Department of Electrical Engineering for its continued support of this research program throughout the years. It was an honor and privilege to work with so many talented minds as President of VC-PERTS. Those friendly working relationships, late nights, and bold engineering endeavors will always be treasured.

Table of Contents

LIST OF TABLES AND FIGURES

PREFACE

No department of applied electricity has undergone greater development during the last two years than that which concerns the use of electricity as a motive power. In America, a remarkable interest in the subject has been manifested, leading from mere experiment in the laboratory to practical work and the opening up of a new occupation for electricians. As a result, several thousand motors are now in successful operation all over the country, while on numerous street railways electricity has become the sole agency of locomotion.

…

It is true that in some minor respects the application of electric motors is still in an experimental state, and that until definite principals and acknowledged standards have been reached, a book on the subject must necessarily be somewhat inclusive. This might, indeed, be said with equal pertinence of the electric light and the telephone. But the authors will be satisfied if they have done something toward the evolution of the perfect motor of the future, and if they have cited enough of the abundant evidence to show that the electric motor and the electric transmission of energy have already won their rightful place in the domain of the arts and sciences. After witnessing the performance of a great variety of motors and traveling on a great many electric railways, they feel justified in their belief that the career of the electric motor begun so auspiciously will in several respects be a counterpart of the now universal steam engine, and that it will realize brilliantly the liberal promise of possibilities still remote.

New York, December, 1886. JOSEPH WETZLER,
THOMAS COMMERFORD MARTIN

—It is remarkable that after centuries of innovation, the search continues for the perfect motor of the future. Quoted from the preface of *The Electric Motor and its Applications*, New York: W.J. Johnston, Publisher, 1887.

NOMENCLATURE

F_k	Propulsion force component produced by phase k	N
F_k^*	Propulsion force command for phase k	N
F_x	Net propulsion force in the longitudinal x-direction	N
F_{CMD}	Net propulsion force command	N
k_{rf}	Coefficient of rolling friction due to the vehicle wheel bearings	$1/s^2$
i_k	Instantaneous current in phase k	A
l_k	Instantaneous flux linkage in phase k	V-s
L_k	Instantaneous mutual inductance in phase k	Henries
$\frac{\partial L}{\partial x}$	Rate of change of inductance in the longitudinal x-direction	N/A^2
$\frac{\partial L}{\partial z}$	Rate of change of inductance in the normal z-direction	N/A^2
M	Mass of the vehicle	Kg
$f_{OPTIMAL}$	Optimal phase selection	
R	Resistance of the phase winding	Ohms
ΔT	Computation time for one iteration of the sensorless algorithm	s
v_k	Instantaneous voltage in phase k	V
V_k	Average value of the phase voltage over one cycle	V
V_{DC}	DC-link voltage	V
v_{ref}	Instantaneous phase voltage command reference	V
v_{ramp}	Instantaneous PWM ramp waveform	V
V_{ramp}	Peak-to-peak magnitude of the PWM ramp waveform	V
x	Position of the vehicle in the longitudinal x-direction	m
x_{ABS}	Estimated absolute position of the vehicle	m
x_{rel-k}	Estimated relative position using phase k	m
x_{LUT}	Estimated position produced by the 2-D position Look Up	m

Chapter 1

INTRODUCTION

Linear Switched Reluctance Machines (LSRMs) are high efficiency, low cost linear actuators suitable for a diverse array of applications such as transit systems, semiconductor manufacturing, elevators, steel mills, material handling and sorting, factory automation, and airport baggage systems. LSRMs are capable of producing straight-line motion directly without linkages, gears, or belts. By applying translation forces directly through the air gap using magnetic fields, much of the hardware found in traditional drive systems is eliminated. The result is lower maintenance costs, improved energy efficiency and less hardware susceptible to wear and tear.

LSRMs are distinguished from other linear actuators by their simple construction, inherent hardware redundancy, relatively simple fault-tolerant control schemes, concentrated windings, and single-sided actuation. This makes LSRMs appealing as actuators for high reliability, low-cost manufacturing applications. A significant drawback of Linear Switched Reluctance Machines and their rotary Switched Reluctance Machine (SRM) counterparts, however, is that they require absolute position and speed feedback, and the phase current must also be measured for propulsion force or torque control. The position/speed transducer and related hardware also has a detrimental impact on the simplicity, cost and reliability of Switched Reluctance Machines. In general, the requirement for a mechanical position transducer has reduced the competitiveness of SRMs compared to linear induction and synchronous machines. Position transducers can be especially expensive in linear machines because the cost and size of the assembly increases in proportion to the length of the machine.

The promise of sensorless positioning is the elimination of the mechanical position sensor assembly and related hardware. Recently, a large body of research has focused on this topic for rotary SRMs. A great variety of methods has been developed to achieve position sensorless operation. The word "sensorless" is actually somewhat of a misnomer since the machine windings themselves are in fact used as position transducers. This decreases the number of components susceptible to wear and tear, reduces the size and weight of the machine, and lowers fabrication and maintenance costs. Such benefits are especially important in large volume applications that are cost sensitive and do not require high performance, such as automotive accessories, household appliances, fans, and pumps [1].

Position sensorless control systems can be implemented using continuous or discrete acquisition, with or without external signal injection. Techniques based in modern control theory include Kalman filters, observers, fuzzy logic, or neural network approaches. These methods can be sensitive to parameter variation and computationally intensive. Other schemes capitalize directly on the position-dependence of the mutual inductance in the phase windings, which can be measured using external signal injection or via the phase currents. For instance, the inductance can be calculated from the inverse time-derivative of the phase currents. Flux linkage can also be used in the same way since it is a related function of position and current. Flux linkage can be calculated by integrating the phase voltages and currents.

This paper involves the development and implementation of a flux linkage based sensorless positioning scheme for a Linear Switched Reluctance Machine. A two-dimensional look up table is used to map the calculated flux linkage and measured phase current to a relative position. Relative position is obtained from the look up table rather than an absolute position because the flux linkage is a

magnetic property that repeats every translator cycle. Chapter 2 of this document summarizes the prototype LSRM machine design and control system. The absolute position of the vehicle translator is found by summing the incremental changes in relative position, and the velocity of the vehicle is the time derivative of its relative position. The goal of this investigation is to explore the addition of sensorless positioning capabilities to an operational LSRM prototype by retrofitting a new system with minimal modifications to the existing DSP-based controller.

In the previously existing prototype, a position sensor on the vehicle reads a magnetic strip on the track to provide position feedback in Quadrature encoder format with a resolution of 10 micrometers. The digital control system uses a TMS320C240 DSP evaluation module with a sampling time of 100 microseconds for force control and 2 milliseconds for velocity control. An external interface board uses control signals from the DSP to generate 10-kilohertz PWM gate drive signals for the converter boards that supply the track windings.

In the proposed sensorless implementation, a data acquisition card and real-time AMD 486 processor are added to the LSRM prototype to estimate the vehicle position based on phase voltages and currents. The output of the system is the absolute vehicle position in Quadrature encoder format. This is interfaced to a counter on the DSP via an interface board that provides the same connections as the mechanical position sensor, but in this case the position is estimated by an add-on computer rather than measured directly.

The result is an "add-on," or "retrofit" sensorless positioning system that emulates the output of the mechanical position sensor. Ideally, little modification of the existing DSP control system would be required using this approach. This novel tactic may be appealing when sensorless positioning capabilities are added to an operational SRM that had previously used a position sensor, and minimal

changes to the control system are desirable. Additional acquisition and processing hardware must be added, however. The approach may not be feasible for all systems, depending on the design of the existing controller. For instance, the proposed scheme is a flux-linkage based method without external signal injection so a current must exist in at least one phase at all times for position estimation. (Since the flux linkage is explicitly zero if the phase current is zero, the flux linkage cannot be used to estimate position without phase current.) In the prototype LSRM, a multiphase excitation scheme is used to produce ripple-free propulsion force so there always exists one or two phases with current at any given time. Each time the sensorless algorithm executes, it uses the phase with maximum current as the "optimal phase" for position estimation.

The principal design goal for the position estimator has to do with the accuracy of the estimated absolute position and velocity. It is also important to update or refresh the estimate rapidly, and to minimize the latency. Table 1 specifies the mechanical sensor performance and two sets of design goals for the sensorless positioning system.

Table 1. Design Specifications

	MECHANICAL	ACCEPTABLE	WORST CASE
Position Accuracy	± 10 micrometers	± 0.5 mm	± 5 mm
Velocity Accuracy	± 0.01 m/sec	± 0.1 m/sec	± 0.5 m/sec
Refresh Rate and Latency	< 1 millisecond	10 milliseconds	100 milliseconds

The salient features of the add-on sensorless position estimator hardware are summarized in Table 2. A real-time embedded computing system by National Instruments, Inc. is used as the data acquisition and computing platform for implementing the sensorless algorithm.

Table 2. Main Features of the Add-On Sensorless Hardware

System / Vendor	LabVIEW™ RT / National Instruments, Inc.
Processor	AMD 486DX5 133 MHz Clock Speed 33 MHz CPU Bus Speed 8 MB User-Programmable DRAM Memory 1 kB SRAM Shared Memory Real-Time Operating System
Data Acquisition Daughter Card	PCI-6040E 16 Single-Ended, 8 Differential Analog Input Channels 250 kS/s Sampling Rate at 12-Bit Resolution 2 Analog Output Channels at 12-Bit Resolution 8 (5 V/TTL) Digital I/O Lines 2 Up/Down, 24-Bit Resolution Counter Timers Analog and Digital Triggering
Digital Inputs (TTL)	Position Index Trigger
12-bit Analog Inputs	Phase Currents (3), Phase Duty Cycles (3), Force Command
Encoder Emulation Circuit Outputs	Encoder Phase A, Encoder Phase B, Encoder Z-Index
Application Software / Programming Language	LabVIEW™ RT for Windows 98 / LabVIEW™ G-Language

This thesis document continues in Chapter 2 with a description of the prototype LSRM machine design, converter and control system. Chapter 3 details the design of the proposed sensorless position estimator. Chapter 4 presents an analysis of the sources of error and their propagation through the sensorless positioning system. Chapter 5 concludes with a summary of the major results and recommendations for future study.

Chapter 2

LSRM MACHINE DESIGN, CONVERTER AND CONTROL

2.1 Background Information

The 4.8-m long Linear Switched Reluctance Machine used in this research was designed and constructed between Jan. and Apr. of 1998 as a joint effort between the Virginia Tech Motion Control Systems Research Group and the student-run Personal Electric Rapid Transit Systems division of the Virginia Tech Virtual Corporation, under the direction of Dr. Krishnan Ramu. The prototype was developed as a proof-of-concept model to demonstrate the feasibility of Linear Switched Reluctance Machines as linear actuators for transportation and a diverse array of other applications. Some of the potential benefits of LSRMs are summarized in Table 3. Although they require position and velocity sensing for control, LSRMs may have significant advantages compared to other configurations such as linear inductance and linear synchronous machines if position and velocity sensing can be accomplished inexpensively.

Table 3. Potential Benefits of LSRMs

	JUSTIFICATION
High efficiency	Small air gap, individual coils excited rather than entire sections of track
High performance	Large force to weight ratio, full propulsion force from standstill, machine can be designed for a large range of acceleration and velocity characteristics
High reliability / low maintenance	Simple construction, few moving parts, passive side requires no electronics, rugged construction
Fault tolerant	Can operate even with a phase shorted or open, inherent hardware redundancy due to multiple coils per phase and multiphase excitation

Low cost construction	Simple geometry yields inexpensive manufacturing, simple individual-unit coil production
Non-distributed windings	Coils are individual units and are not interwoven
Single-sided excitation	Coils are required on only one side of the machine—either track or vehicle

2.2 Prototype LSRM Machine Design

The design procedure for the prototype was presented at the 1999 Industry Applications Society Conference and published in [2]. In this paper, machine design techniques originally developed for rotary SRMs are translated into a procedure suitable for the design of linear SRMs. This procedure was verified by correlating the results from analytical, finite-element, and experimental measurements of properties such as inductance, force, current, and position. The prototype LSRM has a longitudinal flux configuration and is constructed of stacked, insulated M19 steel laminations. The stator, or stationary side, is the active side and has two coils per phase that are connected in series and excited simultaneously. Henceforth in this document, the set of two series-connected coils will be called a single *winding*. The moving side, analogous to the rotor in a rotary SRM, is passive and holds no coils or other electronics except for the mechanical position transducer. The machine has three phases, six translator poles, and 120 stator poles divided into 20 sectors. This geometry is analogous to a 6/4 rotary SRM, but with six translator poles instead of four to prevent the reversal of flux at the instant of phase current commutation, refer to Figure 1 [2]. Important features of the machine design are summarized in Table 4.

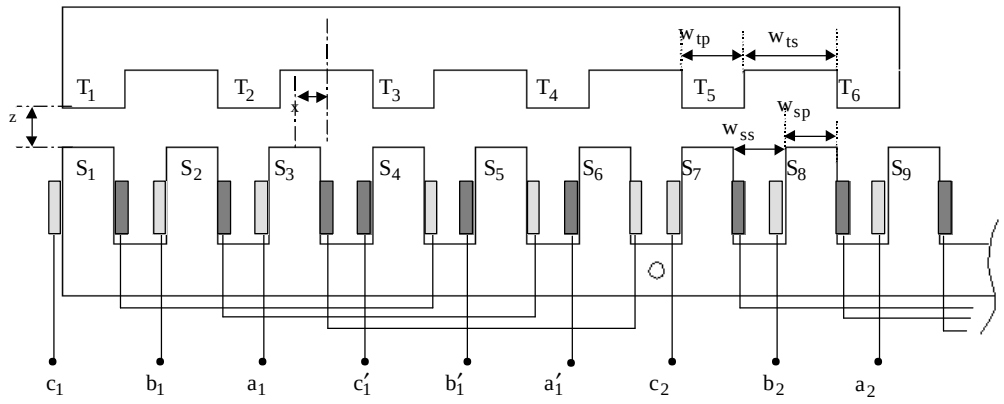

Figure 1. Prototype LSRM Geometry and Phase Winding Configuration (Adapted from [3])

Table 4. Important Features of the Prototype LSRM

SPECIFICATION	VALUE
Track length	4.8 m
Vehicle mass	20 kilograms
Maximum velocity	1.5 m/s
Maximum acceleration	2.25 m/s^2
Maximum propulsion force	45 Newtons
Rated power	200 Watts
Rated phase current	8.5 Amps
Phase inductance range	6.4 to 32 milliHenries
DC-link voltage	85 V
Air gap length	1 millimeter
Stator pole spacing	40 mm
Translator pole spacing	60 mm

2.2.1 Magnetic Characteristics

The magnetic properties of this topology are calculated using Finite Element Analysis (FEA). The flux linkage in phase A is an even function of position and current that repeats every 60 mm and is symmetric about 30 mm, as shown by Figure 2.

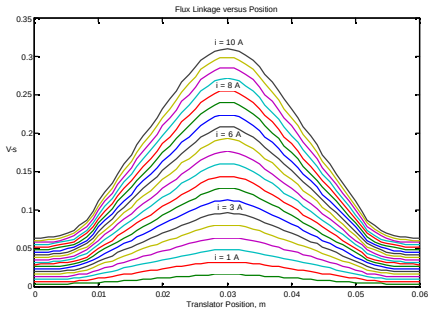

Figure 2. Flux Linkage in Phase A Versus Position and Current

The data is manipulated to form a table that maps flux linkage and current to translator position, forming a two-dimensional array. This Look Up table represents the core element of the sensorless positioning algorithm. Figure 3 illustrates the use of the table to estimate position.

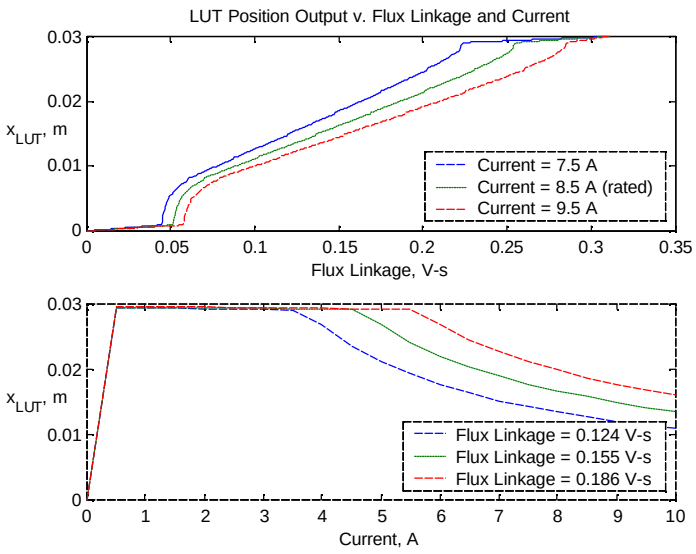

Figure 3. Position Versus Various Values of
Phase A Flux Linkage and Current

2.3 Converter and Control System

In [3], a high-performance control system for the LSRM prototype is presented that provides pulsation-free propulsion force, reduces variation in the normal force, and uses a converter topology that minimizes the number of power electronic switching devices. The translator is mounted to the undercarriage of a wheeled vehicle that rolls freely over the track rails in the longitudinal x-direction, but is not permitted to move in the normal z-direction, see Figure 1. Propulsion force in the desired direction is generated by energizing the appropriate phase winding, depending on the translator position. The magnitude of the propulsion force depends on the phase current and the rate of change of inductance in the longitudinal direction, if the machine is operating with linear magnetic characteristics outside of saturation. By Equation 2.1, the propulsion forces can be produced in either direction, depending on the sign of the rate of change of inductance.

$$F_x = \frac{1}{2} i^2 \frac{\partial L}{\partial x} \tag{2.1}$$

The magnitude of the normal force, which pulls the translator downwards towards the stator, depends on the phase current and rate of change of inductance in the normal direction. Note that due to the squared term in both equations, the sign of the current is irrelevant. In the prototype LSRM, the current is unipolar and flows in one direction only.

$$F_z = \frac{1}{2} i^2 \frac{\partial L}{\partial z} \tag{2.2}$$

The inductance and its spatial rate of change in the x and z-directions are calculated via finite-element analysis and plotted in Figure 4.

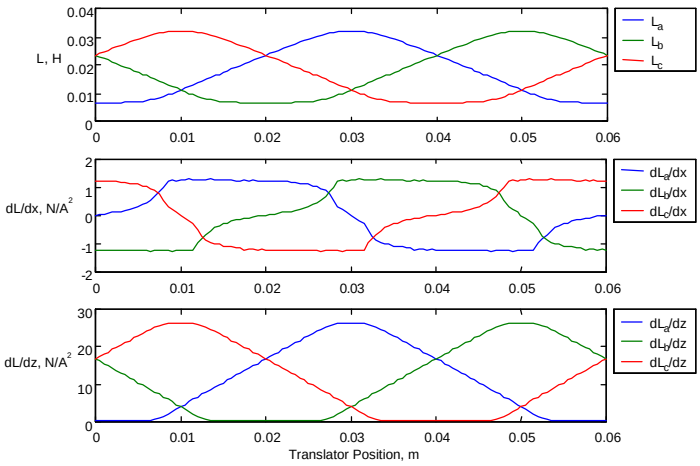

Figure 4. Inductance Profiles for All Three Phases of the LSRM [3]

2.3.1 The Force Distribution Function (FDF)

To prevent propulsion force variations at the instant when each phase is turned on and off, more than one phase winding is energized at a time. This procedure is called multiphase excitation, and the result is that there is always at least one phase that is energized and has a nonzero phase current, so the propulsion force never goes to zero. A Force Distribution Function (FDF) is used to distribute the propulsion force among the three phases as the vehicle travels. The FDF ensures that the sum of forces among the three phases is equal to the force command, and provides a smooth transition between the phases. The FDF algorithm is described in more detail later in this chapter.

2.3.2 Current Command Generation

Another function, called the Current Command Generation Function (CCG) is used to calculate the amount of current required to generate the desired propulsion force in each phase.

$$i = \sqrt{\frac{2F_x}{\frac{\partial L}{\partial x}}} \tag{2.3}$$

2.3.3 Vehicle Motion Simulation

To foster the development of the sensorless positioning scheme, two simulation models were built using the Simulink toolbox for Matlab®. The first is a vehicle motion simulation, intended to simulate: (1) the physical dynamics of the vehicle mass with rolling friction, (2) the velocity and position feedback loops, (3) the Force Distribution Function, and (4) the current command generation functions. The operation of the Force Distribution Function is shown in the simulation results of Figure 5 below. In this simulation, the vehicle accelerates at approximately 1 m/s^2 from a standstill when given a force command at 0.1 seconds. The simulation model is shown in Figure 6.

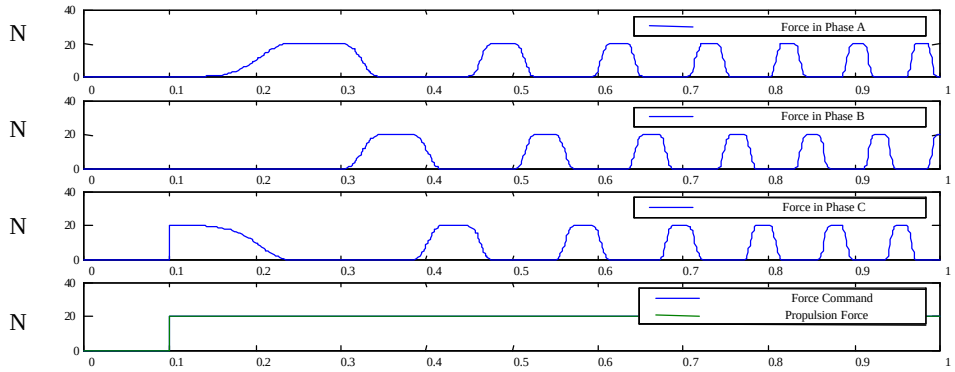

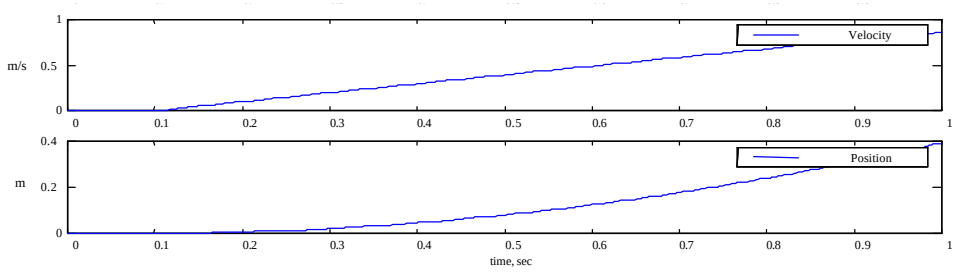

Figure 5. Simulation Results Showing Operation of the Force Distribution Function

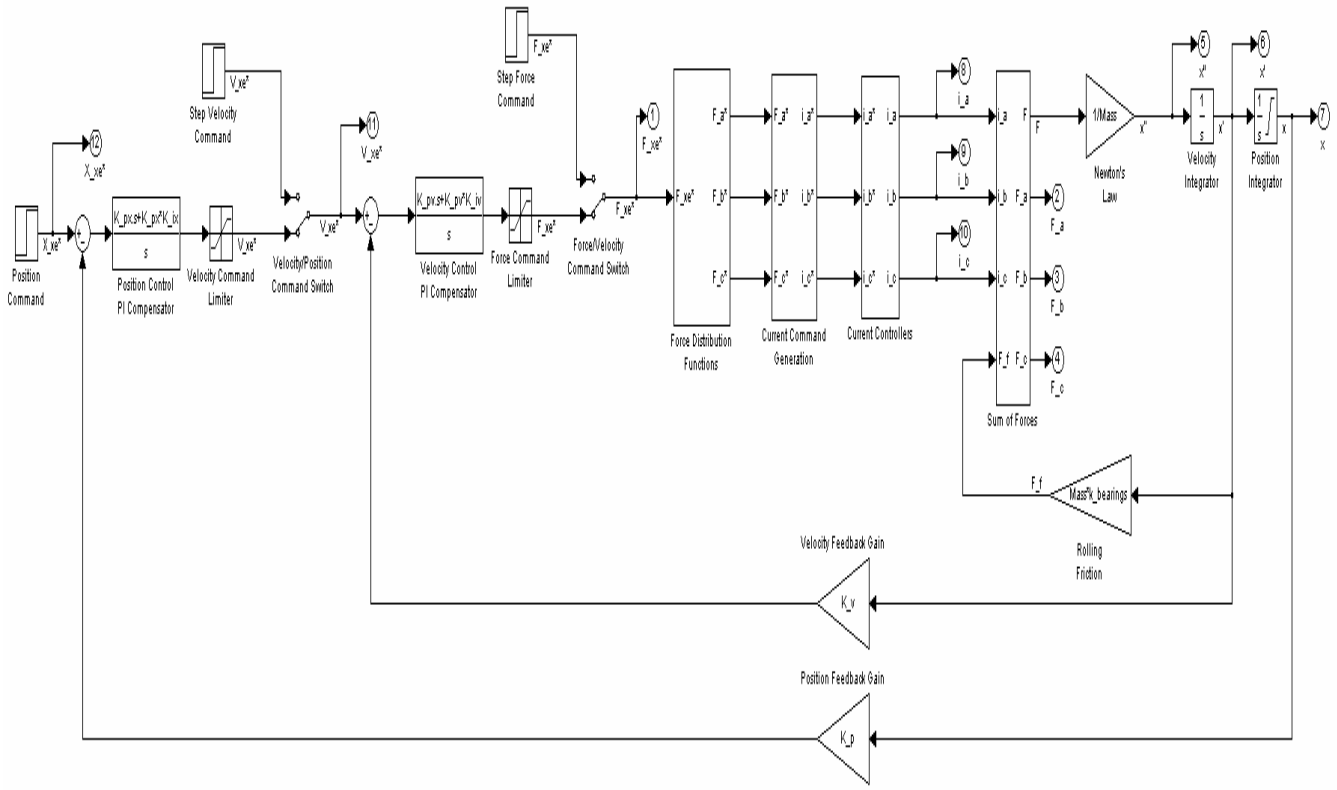

Figure 6. Vehicle Motion Simulation Model

2.3.4 Vehicle Dynamics

The vehicle plant is modeled as a mass with rolling friction and one-degree of freedom in the longitudinal direction. An equation for the acceleration of the vehicle is written from Newton's law; where M is the mass of the vehicle, k_{rf} is the coefficient of rolling friction, and F_a, F_b, F_c, are the propulsion forces generated by each of the phase windings. Note that static friction and the nonlinear dynamics during the moment of transition from rest to motion are neglected.

$$\frac{d^2x}{dt^2} = \frac{1}{M}\left(F_{x-A} + F_{x-B} + F_{x-C}\right) - M \cdot k_{rf}\,\frac{dx}{dt} \tag{2.4}$$

2.3.5 Converter Simulation

A second Simulink model was also developed to focus on the current control loop and the power electronics. This model was designed to represent the operation of the DSP-based control system; so the sensorless algorithm could be developed and tested in a realistic context prior to hardware implementation. The major components of the model are, (1) the Force Distribution and Current Command Generation Functions, (2) the phase winding dynamics with position-dependent inductance, (3) the Proportional-Integral (PI) current control feedback loop including anti-windup PWM generation, (4) the novel unipolar switching converter topology, and (5) the flux-linkage based sensorless position estimator. The simulation assumes a fixed vehicle velocity and uses Look Up tables to calculate position-dependent magnetic properties such as the phase inductances and their spatial derivatives at each simulation step. The model uses built-in functions such as integrators, as well as customized S-Functions written in Matlab

code to implement more complicated non-linear functions such as the Force Distribution Function.

2.3.6 The FDF S-Function

The propulsion Force Distribution Function is summarized in Table 5. Note that the function depends on position, the longitudinal rate of change of the phase inductances, and the force command.

Table 5. Propulsion Force Distribution Function

TRANSLATOR POSITION (mm)	FORCE COMMAND (N) $F_{CMD} \geq 0$	FORCE COMMAND (N) $F_{CMD} < 0$
$0 \leq x < 10\,\text{mm}$	$F_A^* = \dfrac{F_{CMD}\left(\dfrac{\partial L_A}{\partial x}\right)^2}{\left(\dfrac{\partial L_A}{\partial x}\right)^2 + \left(\dfrac{\partial L_C}{\partial x}\right)^2}$ $F_B^* = 0$ $F_C^* = \dfrac{F_{CMD}\left(\dfrac{\partial L_C}{\partial x}\right)^2}{\left(\dfrac{\partial L_A}{\partial x}\right)^2 + \left(\dfrac{\partial L_C}{\partial x}\right)^2}$	$F_A^* = 0$ $F_B^* = F_{CMD}$ $F_C^* = 0$
$10 \leq x < 20\,\text{mm}$	$F_A^* = F_{CMD}$ $F_B^* = 0$ $F_C^* = 0$	$F_A^* = 0$ $F_B^* = \dfrac{F_{CMD}\left(\dfrac{\partial L_B}{\partial x}\right)^2}{\left(\dfrac{\partial L_B}{\partial x}\right)^2 + \left(\dfrac{\partial L_C}{\partial x}\right)^2}$ $F_C^* = \dfrac{F_{CMD}\left(\dfrac{\partial L_C}{\partial x}\right)^2}{\left(\dfrac{\partial L_B}{\partial x}\right)^2 + \left(\dfrac{\partial L_C}{\partial x}\right)^2}$

$20 \le x < 30\,\text{mm}$	$F_A^* = \dfrac{F_{CMD}\left(\dfrac{\partial L_A}{\partial x}\right)^2}{\left(\dfrac{\partial L_A}{\partial x}\right)^2 + \left(\dfrac{\partial L_B}{\partial x}\right)^2}$ $F_B^* = \dfrac{F_{CMD}\left(\dfrac{\partial L_B}{\partial x}\right)^2}{\left(\dfrac{\partial L_A}{\partial x}\right)^2 + \left(\dfrac{\partial L_B}{\partial x}\right)^2}$ $F_C^* = 0$	$F_A^* = 0$ $F_B^* = 0$ $F_C^* = F_{CMD}$
$30 \le x < 40\,\text{mm}$	$F_A^* = 0$ $F_B^* = F_{CMD}$ $F_C^* = 0$	$F_A^* = \dfrac{F_{CMD}\left(\dfrac{\partial L_A}{\partial x}\right)^2}{\left(\dfrac{\partial L_A}{\partial x}\right)^2 + \left(\dfrac{\partial L_C}{\partial x}\right)^2}$ $F_B^* = 0$ $F_C^* = \dfrac{F_{CMD}\left(\dfrac{\partial L_C}{\partial x}\right)^2}{\left(\dfrac{\partial L_A}{\partial x}\right)^2 + \left(\dfrac{\partial L_C}{\partial x}\right)^2}$
$40 \le x < 50\,\text{mm}$	$F_A^* = 0$ $F_B^* = \dfrac{F_{CMD}\left(\dfrac{\partial L_B}{\partial x}\right)^2}{\left(\dfrac{\partial L_B}{\partial x}\right)^2 + \left(\dfrac{\partial L_C}{\partial x}\right)^2}$ $F_C^* = \dfrac{F_{CMD}\left(\dfrac{\partial L_C}{\partial x}\right)^2}{\left(\dfrac{\partial L_B}{\partial x}\right)^2 + \left(\dfrac{\partial L_C}{\partial x}\right)^2}$	$F_A^* = F_{CMD}$ $F_B^* = 0$ $F_C^* = 0$

$50 \leq x < 60$ mm	$F_A^* = 0$ $F_B^* = 0$ $F_C^* = F_{CMD}$	$F_A^* = \frac{F_{CMD}\left(\frac{\partial L_A}{\partial x}\right)^2}{\left(\frac{\partial L_A}{\partial x}\right)^2 + \left(\frac{\partial L_B}{\partial x}\right)^2}$ $F_B^* = \frac{F_{CMD}\left(\frac{\partial L_B}{\partial x}\right)^2}{\left(\frac{\partial L_A}{\partial x}\right)^2 + \left(\frac{\partial L_B}{\partial x}\right)^2}$ $F_C^* = 0$

2.3.7 Phase Windings with Position-Dependent Inductance

The phase windings, or sets of two series-connected coils, are also simulated using an S-Function. Because the vehicle is in motion, the inductance of the winding varies as the translator position changes. The windings are modeled using a time-varying state-space model. In Equation 2.5, the coil dynamics are expressed as a time-domain differential equation.

$$v_k(t) = R \cdot i_k(t) + L_k(t)\frac{\partial i_k(t)}{\partial t} + i_k(t)\frac{\partial L_k(t)}{\partial t} \tag{2.5}$$

This can be transformed into a SISO state-space model with voltage as the input and current as the output. Note that the resistance is considered a constant. The inductance and its time-derivative are passed as parameters to the S-Function at each simulation step.

$$\frac{\partial i_k(t)}{\partial t} = \left[-\frac{R + \frac{\partial L_k(t)}{\partial t}}{L_k} \right] i_k(t) + \left[\frac{1}{L_k} \right] v_k(t) \tag{2.6}$$

$$y(t) = i_k(t)$$

2.3.8 PI Current Control Compensator

The Proportional-Integral (PI) current control compensator including anti-windup is modeled using built-in Simulink blocks. The compensator includes an anti-windup feature that tends to pull the integrator out of saturation. If the duty-cycle command exceeds the ± 95% limitation, the difference is fed back into the integrator to decrease its output. The integral component also has a reset, which occurs whenever the phase current command transitions to and from zero.

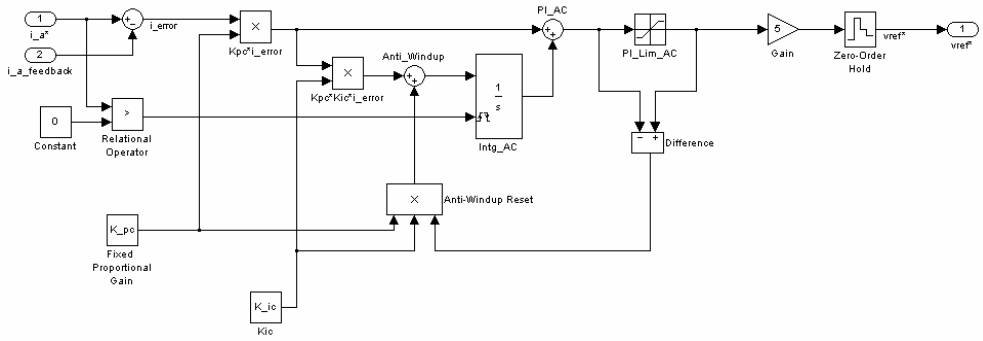

Figure 7. Proportional-Integral (PI) Current Control Compensator with Anti-Windup

2.3.9 Converter Topology

The full-bridge asymmetric converter topology used in the prototype LSRM is detailed in [3]. Only one upper switch for each of the three phases is required, plus one lower switch for each individual phase winding. A single current sensor to detect the phase current is connected in series with each of the

upper switches; so only three current sensors are required for the entire track, as in Figure 8. Four galvanically isolated current transducers are used in the LSRM prototype, with the fourth sensor utilized by an alarm subsystem to detect over-current and under-current conditions.

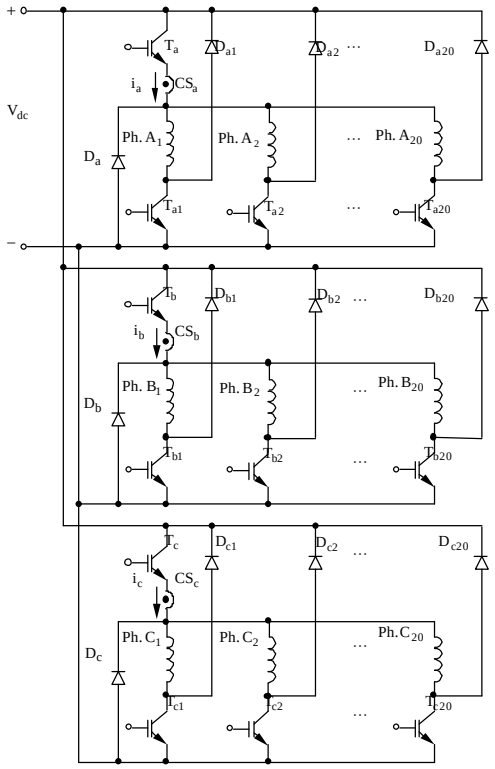

Figure 8. Prototype LSRM Converter Topology
(Adapted from 3)

2.3.10 Unipolar Switching Strategy

A modification of the unipolar switching strategy proposed in [6] is selected due to its good frequency response and low current ripple. Although four-quadrant operation is possible, only two-quadrant operation is required for the prototype. The unipolar switching algorithm is simulated via an S-Function that implements Equation 2.7.

$$v_k(t) = \begin{cases} V_{DC} & \text{if } v_{ref} \geq v_{ramp} \text{ and } -v_{ref} < v_{ramp} \\ -V_{DC} & \text{if } v_{ref} < v_{ramp} \text{ and } -v_{ref} \geq v_{ramp} \text{ and } i_k > 0 \\ 0 & \text{otherwise} \end{cases} \quad (2.7)$$

The unipolar S-function uses the duty cycle voltage reference produced by the current control compensator. This command is compared to an externally generated ramp waveform to time the opening and closing of the gates of the converter. The resultant phase voltage is a Pulse Width Modulated (PWM) signal with a magnitude equal to the DC link voltage, an average value and duty cycle proportional to the reference voltage, and a frequency equal to that of the ramp waveform.

In the prototype, the reference voltage is produced by the DSP current control compensator and is output as a digital instruction word, PWM^*. This instruction word also indicates which winding or windings on the track should be excited, depending on the translator position. Because a maximum of two phases are excited at a given time, only two voltage reference signals are actually produced to minimize the length. Programmable logic devices on an external interface board interpret the instruction and generate the appropriate gating signals for the converter boards.

2.3.11 Flux Linkage Estimation via Integration

One drawback of this topology from the perspective of a flux linkage based sensorless algorithm is that the phase voltage cannot be measured without one voltage sensor per winding. This is problematic because phase voltage is required to calculate the flux linkage via integration using Faraday's Law, as in Equation 2.8. Note that the phase voltage is the most important term in this equation because its magnitude is much large than the phase current and winding resistance.

$$l_k(t) = \int v_k(t) - R \cdot i_k(t) dt \tag{2.8}$$

Since there are 20 sectors with three windings per sector in the prototype LSRM, 60 voltage sensors would be required. The sensors would probably need galvanic isolation to protect the low-voltage digital electronics of the estimator because of the relatively high voltage in the phase windings. These voltage sensors would be a significant addition of expensive hardware that might substantially mitigate the proposed benefits of sensorless positioning. Another problem is that the phase voltage is a PWM signal that would be difficult to integrate through direct data acquisition. The exact instant of the rising and falling edges of the phase voltage signal will shift in time depending on the duty cycle and ramp waveform, due to the nature of the unipolar switching algorithm. It would be very difficult to capture the exact timing of the signal's rising and falling edges. If the duty cycle is small, the phase voltage pulse width could be very short, such as five percent of the switching period. To properly sample such a signal, according to the Nyquist criterion, would require an acquisition rate as high as 40 times the switching frequency. Both high-bandwidth voltage sensors and high-speed acquisition hardware would be required. If an analog low-pass filter were used to give the average value over one switching cycle, the output of the filter could be sampled at just twice the switching frequency to satisfy Nyquist. However, the addition of such a filter to each voltage sensor would only increase the amount of hardware required.

An alternative approach would use the voltage reference signal produced by the current control compensator. The voltage reference is a zero-order hold signal that is updated only once per switching cycle. If the converter is operating properly, this signal should be proportional to a zero-order hold equivalent of an analog low pass filter described. The average value of the phase voltage over one

switching cycle depends on the voltage reference and the magnitude of the DC-link voltage.

$$V_k = v_{ref-k} \cdot V_{DC} \tag{2.9}$$

Although indirect, this approach may have some advantageous because the number of voltage reference outputs from the DSP required to make this signal available to the external position estimator is equal to the maximum number of phases excited at any given time; in this case two. Also, the integration of a zero-order hold signal is relatively straightforward and can be accomplished with a sampling frequency equal to the switching frequency if a trigger signal is used to time the acquisitions. In this case, such a trigger signal is unavailable so the maximum sampling rate of the sensorless estimator given computational constraints is 10,000 samples per second.

Chapter 3

DESIGN OF THE SENSORLESS POSITION ESTIMATOR

3.1 Background Information

A large variety of methods have been proposed for the sensorless estimation of position in rotary Switched Reluctance Machines (SRMs). However, little research exists regarding sensorless estimation for Linear SRMs. Fortunately, most of the results that apply to rotary machines are applicable to their linear counterparts. The principal difference between linear and rotary estimation schemes stems from the fact that the number of phase windings and switching devices in a linear machine may be much larger than in a rotary machine. If the active side of the machine is on the track, the number of devices increases in proportion with the length of track. Measuring the phase voltage directly may be problematic, since one voltage sensor per phase winding would be required. By the same reasoning, it may not be cost effective to use a sensorless approach involving signal injection, since the amount of additional hardware required for the sensorless algorithm would also be proportional to the length of track.

The rotary motor sensorless schemes proposed in literature can be categorized by, (1) the method in which the position-dependent magnetic properties are measured (measurement technique), and (2) the way in which this information is used to compute position (computational technique). Many combinations and permutations of measurement and computational techniques have been examined [52, 53, 54, 59].

Most sensorless methods capitalize directly on the position-dependent magnetic characteristics of the machine, namely the inductance or its flux-linkage counterpart. Inductance and flux linkage are related in Equation 3.10. Note that the inductance is written as a function of current, which is true if the machine is operating in saturation. If the machine is not in saturation and mutual coupling between the phases is neglected, the inductance is purely position dependent. Also, the relationship between inductance and position does not depend on speed if back-emf effects are neglected. The next section contains a review of various methods to measure or estimate position dependent magnetic properties.

$$l_k(x,i,t) = L_k(x,i) \cdot i_k(t) \tag{3.10}$$

3.1.1 Measurement of Magnetic Properties

There are a large number of methods that may be implemented to measure or estimate the position dependent machine properties such as the self-inductance, mutual inductance, and flux linkage. These techniques use measurements that are acquired continuously or at discrete intervals, using active or inactive phase. Although discrete methods are often simpler to implement, they may generate an undesirable negative torque as they often involve the excitation of an inactive phase in the negative inductance slope region. Also, discrete methods may not function at high speed due to the time required for each acquisition. When using an active phase approach, the existing voltage and current signals due to the normal commutation of the machine are measured. Examples of such non-intrusive approaches include observer based techniques [55], the flux/current method, and the mutual voltage technique [26, 37, 56, 63]. If an inactive phase is used, diagnostic signals are injected by the converter or by a low-voltage analog circuit. Active probing methods include current waveform methods, amplitude/frequency modulation techniques, and flux sensing

techniques. The mathematical basis of several common methods is reviewed below, although many variations of the relevant equations exist in practice.

3.1.1.1 Discrete Acquisition

In a phase pulsing scheme [13, 44, 60, 62], a voltage pulse is applied to an unenergized winding for a fixed period of time and the resultant change in current is measured, yielding a discrete inductance or incremental inductance estimate via Equation 3.11.

$$L = V\frac{\Delta T}{\Delta I} \tag{3.11}$$

Current rise time [20, 21, 45, 46, 48, 61] and current fall time [14, 41, 48] schemes are non-intrusive variations of the phase pulsing scheme, but they use the voltage on and off times of an active phase and the incremental change in current during the switching cycle. Equation 3.12 gives the incremental inductance equations for the current rise time and current fall time approaches respectively. Note the inclusion of an induced or motional emf term, e, which complicates this approach.

$$e = \frac{\partial l}{\partial x}\frac{\partial x}{\partial t}$$

$$dL = \frac{\partial l}{\partial i} = \begin{cases} \dfrac{V - R \cdot I - e}{\Delta I}\Delta T & \text{(Current Rise Time)} \\ \text{or} & \\ \dfrac{-R \cdot I - e}{-\Delta I}\Delta T & \text{(Current Fall Time)} \end{cases} \tag{3.12}$$

3.1.1.2 Continuous Acquisition

In a frequency modulation scheme [19, 43, 49, 64], a low-voltage analog circuit is used to sense the inductance of an inactive phase via signal injection and to generate a train of square wave signals whose frequency is proportional to the instantaneous inductance. The frequency-modulated signal produced can then be decoded by a Frequency-to-Voltage (F-V) Converter or via software.

In a phase modulation scheme [42], a sinusoidal voltage of frequency ? is injected and the phase angle difference, F, at the resulting current response is used to estimate the inductance via Equation 3.13.

$$L = R\frac{\tan \Phi}{w} \tag{3.13}$$

In an amplitude modulation scheme [32, 40, 43, 48, 49], the amplitude of the current, I_m, is used to indicate the inductance, where V_m is the amplitude of the injected sinusoidal voltage.

$$L = \frac{1}{w}\sqrt{\frac{V_m^2}{I_m^2} - R^2} \tag{3.14}$$

In a flux/current or self-voltage scheme [27, 33, 36, 49, 50], an external signal is usually not injected. Instead, the inductance of an active phase is estimated continuously from the measured phase current and calculated phase flux, as in Equation 3.15.

$$L(t) = \frac{1}{i(t)}\int v(t) - R \cdot i(t)dt \tag{3.15}$$

The flux/current approach is utilized in this study because it does not require signal injection, which would imply significant modifications to the existing DSP controller. Also, the flux/current approach permits the inductance to be estimated continuously and independently since the phase current and voltage signals can be acquired asynchronously with respect to the DSP controller.

3.1.2 Computation of Position

A vast array of computational techniques, algorithms, and error reduction methods have been proposed in recent years. These can be categorized as using modern control/model-based estimator techniques [32, 36], using intelligent control techniques, using vector [35] or direct torque control [17, 18, 38, 42], or using an inverse mapping function that relates a magnetic property back to position.

Modern control techniques include the use of a state observer, or Kalman filter [7, 8, 15]. The observer and Kalman filter approaches estimate rotor position based on a mathematical model of the machine and measured signals, such as the phase current. These approaches can be computationally intensive, so an oversimplified model may be needed that does not include effects such as mutual inductance and saturation. Another drawback of these approaches is that its performance may suffer due to variation in the machine parameters and be sensitive to noise. Also, start-up sequences to initialize the estimated position may be unavailable and initial convergence behavior may be poor.

Neural [11, 16, 30, 31, 34, 39] and fuzzy [9, 10, 25, 28, 29] methods are intelligent control techniques that eliminate the need for a mathematical model of the machine and the measurement noise. However, a long training and learning

phase may be needed to obtain the machine-specific data required for control. During the learning phase, a mechanical position encoder is often required.

Techniques using an inverse mapping function are the most commonly used approaches due to their simplicity. If the position-dependent magnetic properties are measured, the position can also be estimated since the properties are unique over half the rotor/translator cycle. Usually, the magnetic properties are calculated first and then mapped to rotor position. The function that maps the magnetic property to position may be computed *a priori* or in real time. Several forms of an inverse mapping function using different magnetic properties is given in Equation 3.16, where F^{-1} is a function that maps inductance to position, L_k is the self inductance of phase k, dL_k is the incremental inductance of phase k, $?_k$ is the flux linkage of phase k, and M_{kj} is the mutual inductance of phase k and j. Alternately, a model-based estimator scheme can be used to estimate position directly from measured waveforms without first calculating a magnetic property.

$$x = \begin{cases} F^{-1}(L_k) & \text{where } L_k = F(x) \\ \text{or} & \\ F^{-1}(dL_k) & \text{where } dL_k = F(x) \\ \text{or} & \\ F^{-1}(l_k) & \text{where } l_k = F(x) \\ \text{or} & \\ F^{-1}(M_{kj}) & \text{where } M_{kj} = F(x) \end{cases} \tag{3.16}$$

3.2 Proposed Estimation Scheme

The estimation scheme proposed for the Linear Switched Reluctance Machine (LSRM) is similar in many ways to a flux/current method for rotary SRMs. It uses the voltage and current in the active phases to calculate flux

linkage, and then maps the flux linkage and current back to position using a 2-dimensional Look Up Table (LUT). The primary advantage of this approach would be that the normal operation of the high-performance (i.e. force ripple minimization) control system would not be disturbed, so it may be possible to add sensorless positioning capabilities to an existing transducer-based controller. However, it is found that certain control characteristics such as velocity control may be incompatible, so changes may in fact be necessary for successful implementation.

The proposed scheme does not use signal injection, but instead capitalizes on the fact that there is always voltage and current in at least one phase due to multiphase excitation. Thus, the flux linkage can be estimated at all times. The operation of the DSP-based control system for the LSRM relies heavily on Look Up Tables that encapsulate the magnetic properties of the machine. Both the Force Distribution Function and the Current Command Generation functions use a table that encapsulates the longitudinal rate of change of inductance, $\partial L/\partial x$. This table is formed from inductance data generated via Finite Element Analysis (FEA), interpolated to improve its resolution, and then stored in memory for use by the DSP.

Similarly, the proposed estimation scheme uses a Look Up table that maps flux linkage and current to relative position. The main advantage of a table-based approach is that most of the computational effort is done in advance during the formation of the LUT rather than real-time. Indexing the table is a very fast operation, although storage of the table does require memory resources. With this approach, the computational complexity and thereby the cost of the processor is reduced.

3.2.1 The Deterministic Behavior of the DSP

An important characteristic of the LSRM system is the fact that much of the DSP's behavior is predictable and partially controllable. Most of the DSP's operation depends on the position and velocity of the vehicle. While this observation is rather straightforward, its ramifications are far reaching. For example, if the absolute position of the vehicle and the force command is known, one also knows exactly which winding or windings will be excited by the DSP. Thus, it is not necessary to explicitly transmit this information from the DSP to the sensorless system. The interface hardware required to implement the sensorless algorithm is therefore not extensive. Another implication is that the sensorless system can control which windings are excited simply by controlling the absolute position and velocity information stored in the DSP. This capability can be used to develop a start-up search procedure that allows the vehicle to be located via sensorless methods at any arbitrary location on the track. Without a start-up search procedure, a mechanical index sensor must be used to initialize the absolute position at startup. Since the vehicle must be moved over the reset sensor, human intervention is required for start up with a mechanical position sensor.

3.2.2 The Position Look Up Table (LUT)

At the heart of the proposed scheme lies the position Look Up table (LUT), which is constructed as follows. First, the flux linkage properties of the machine at 0.5 Amp intervals of current and 1 millimeter intervals of position are computed via Finite Element Analysis. A software package called Flux 2-D by Magsoft® is used for this purpose. Then a Matlab® script is written to, (1) scale and increase the resolution of the table via interpolation so integer indexes can be used, and (2) invert the table so it can be indexed with flux linkage and current to yield position. The phase currents used to index the table are measured directly,

scaled by the A/D converter, and rounded during their conversion from floating-point to integer format. The flux linkage index is also scaled and rounded, but it is not directly measurable so its value is estimated via an algorithm described below. The resolution of the position estimation might be improved by interpolating between table values in real-time, but this approach is rejected because it would slow the process. The interpolation is done in advance, increasing the memory requirements for the table but improving speed. Although the flux linkage function is different for each of the three phases, only one Look Up table is required. The use of only one table is accomplished by adding an offset, depending on which phase is being used to estimate the position and the sign of the force command.

Since the relationship between flux linkage and position is unique over only half of the 60-millimeter translator cycle, it is also necessary to distinguish which half of the cycle. This can be done by using the sign of the force command, since the command is used by the Force Distribution Function to determine whether the phase should be excited in the first half cycle to produce a positive force, or in the second half cycle to produce a negative force. The sign of the force command determines when the coils are excited during the translator cycle, as indicated in Table 5. Note that the notation $\mathrm{mod}(x,y)$ refers to remainder of x/y when the quotient is rounded toward minus infinity.

$$
\begin{aligned}
x_{rel-A} &= \begin{cases} \mathrm{mod}(0.06 - x_{LUT}(i_A,\ l_{\mathrm{A}}),0.06) & \text{if } F_{CMD} \geq 0 \text{ and } i_A > 0 \\ \mathrm{mod}(x_{LUT}(i_A,\ l_{\mathrm{A}}),0.06) & \text{if } F_{CMD} < 0 \text{ and } i_A > 0 \end{cases} \\
x_{rel-B} &= \begin{cases} \mathrm{mod}(0.08 - x_{LUT}(i_B,\ l_{\mathrm{B}}),0.06) & \text{if } F_{CMD} \geq 0 \text{ and } i_B > 0 \\ \mathrm{mod}(0.02 + x_{LUT}(i_B,\ l_{\mathrm{B}}),0.06) & \text{if } F_{CMD} < 0 \text{ and } i_B > 0 \end{cases} \\
x_{rel-C} &= \begin{cases} \mathrm{mod}(0.10 - x_{LUT}(i_C,\ l_{\mathrm{C}}),0.06) & \text{if } F_{CMD} \geq 0 \text{ and } i_C > 0 \\ \mathrm{mod}(0.04 + x_{LUT}(i_C,\ l_{\mathrm{C}}),0.06) & \text{if } F_{CMD} < 0 \text{ and } i_C > 0 \end{cases}
\end{aligned}
\tag{3.17}
$$

3.2.3 Optimal Phase Selection

Because more than one phase may have current at any given time, the sensorless algorithm must determine which phase should be used to estimate the position. Phase current is chosen for the arbitration variable, since it is measured rather than estimated. By Equation 3.10, the current is also proportionally related to the flux linkage. It is assumed that larger values of flux linkage will tend to be less sensitive to error sources such as measurement noise; so using the phase with maximum current seems sensible. It is also necessary to know the commutation angle, or whether the coils are being excited in the first half of the cycle or the second. The DSP uses the sign of the force command for this purpose. The selection of the optimal phase is accomplished as follows.

$$f_{OPTIMAL} = \begin{cases} \mathrm{A}_{\mathrm{FOR}} & \text{if } i_a > i_b \text{ and } i_a > i_c \text{ and } F_{CMD} \geq 0 \\ \mathrm{A}_{\mathrm{REV}} & \text{if } i_a > i_b \text{ and } i_a > i_c \text{ and } F_{CMD} < 0 \\ \mathrm{B}_{\mathrm{FOR}} & \text{if } i_b > i_a \text{ and } i_b > i_c \text{ and } F_{CMD} \geq 0 \\ \mathrm{B}_{\mathrm{REV}} & \text{if } i_b > i_a \text{ and } i_b > i_c \text{ and } F_{CMD} < 0 \\ \mathrm{C}_{\mathrm{FOR}} & \text{if } i_c > i_a \text{ and } i_c > i_b \text{ and } F_{CMD} \geq 0 \\ \mathrm{C}_{\mathrm{REV}} & \text{if } i_c > i_a \text{ and } i_c > i_b \text{ and } F_{CMD} < 0 \end{cases} \tag{3.18}$$

When the force command changes sign, the new commutation angle will cause a negative force to be produced by the windings but the vehicle will continue to travel in the previous direction for some time. Thus, the force command used by the optimal phase selector must be latched at its previous value until the vehicle comes to a stop. This prevents an incorrect reversal of estimated velocity when the force command changes sign.

3.2.4 Flux Linkage Calculation

Another critical component of the proposed sensorless scheme is the flux linkage calculation algorithm. The motor voltage equation is computed from

Faraday's Law using a trapezoidal integration approach. Note that the DC-link voltage, V_{DC}, and the phase resistance, R, are assumed to be constant.

$$\begin{aligned} l_k(0) &= 0 \\ l_k(n) &= l_k(n-1) + \\ &\frac{\Delta T}{2}\left(V_{DC} \cdot v_{ref-k}(n) + V_{DC} \cdot v_{ref-k}(n-1) - R \cdot i_k(n) - R \cdot i_k(n-1)\right) \end{aligned} \tag{3.19}$$

Ideally, the reference voltages and currents would be sampled once per switching cycle with this approach. In practice, however, they are undersampled since the sensorless processor is not able to achieve the required rate of speed. This introduces error, which is further compounded by factors such as measurement noise, mutual coupling between the phases, and back emf. It is important to reset the integration frequently to prevent the error from building over time. However, since the phase voltage command rather than the true phase voltage is used, the integration tends to reset itself since the voltage reference is held at its full negative value once the phase current reaches zero. This is to prevent the excitation of inactive phases. If the flux linkage is limited to a minimum value of zero, the reset is performed automatically due to the large negative value of the voltage reference. Fortunately, this occurs often since each phase is excited only for about 30 mm of travel, after which the current is driven to zero and the phase becomes inactive.

It is also known that the flux linkage for the machine must lie within a specific range of values, which depend on the particular magnetic characteristics of the machine and the maximum phase current. The values for the maximum and minimum flux linkage are known from Finite Element Analysis and can be used to constrain the flux linkage integration as follows. Although the minimum flux linkage will be identically zero in the case of zero current, an assumption is

made regarding the maximum flux linkage which is assumed to be a constant and not dependent on factors such as current or position.

$$\begin{aligned} &\lambda_k(n) = \lambda_{MAX} \quad \text{if } \lambda_k(n) > \lambda_{MAX} \\ &\lambda_k(n) = \lambda_{MIN} \quad \text{if } \lambda_k(n) < \lambda_{MIN} \\ &\text{where } \lambda_{MIN} = 0\,\text{V}\cdot\text{s},\ \lambda_{MAX} = 0.31\,\text{V}\cdot\text{s} \end{aligned} \tag{3.20}$$

3.2.5 Conversion from Relative to Absolute Position

Although the position LUT can estimate the relative translator position within the translator cycle, it is not able to directly determine the translator's absolute position. The inductive magnetic properties of the machine repeat every 60 mm, so it is impossible to distinguish one sector from another using relative position alone. A simple way to overcome the problem is to keep a running total based on the incremental change in relative position. However, the relative position signal resembles a ramp-waveform that cycles back to zero after every 60 mm of travel. The incremental change in relative position at this instant is ±60 mm, so the incremental change in relative position cannot be used to update the absolute position at this time. However, since the vehicle motion behaves similar to a low pass filter it is unlikely that the velocity of the vehicle will change significantly at this instant. The vehicle velocity prior to the relative position "rollover" is used to compute the incremental change in position for this calculation. This approach is preferred over a traditional digital filter such as the Auto-Regressive Moving Average (ARMA), because the time delay produced is only that of a single computation. The maximum rated vehicle velocity of 1.5 m/s is used to determine when the rollover event has occurred. The absolute position algorithm is as follows. For convenience, the vehicle velocity, $\frac{dx}{dt}$, will hereafter be written as *vel*.

$$x_{ABS}(0) = x_{INITIAL}$$

$$x_{ABS}(n) = \begin{cases} x_{ABS}(n) + x_{REL}(n) - x_{REL}(n-1) & \text{if } \left|\frac{x_{REL}(n) - x_{REL}(n-1)}{\Delta T}\right| < vel_{MAX} \\ x_{ABS}(n) + vel(n-1) \cdot \Delta T & \text{otherwise} \end{cases} \quad (3.21)$$

This "running-total" approach is appealing due to its simplicity, but it does have drawbacks. Over time, error will build and the absolute position will drift further and further from the correct value. This problem can be reduced but not eliminated by improving the accuracy of the relative position estimate. Also, the absolute position could be reinitialized by repeating the start-up sequence. For continuous operation, it may be necessary to implement a method to actively remove the error while the system is in operation, or an alternative approach to the computation of absolute position may be required.

3.2.6 Velocity Estimation

Velocity estimation is an important aspect of the sensorless algorithm because the DSP includes a velocity control loop. The DSP internally computes the velocity using the derivative of the absolute position. Thus, it is important not only that the sensorless position estimate be accurate, but also its rate of change. The proposed estimator must output a Quadrature position signal with a count equal to the absolute position and a rate of change equal to the velocity divided by the encoder resolution. The change in estimated absolute position can be used to estimate the velocity, but it is necessary to filter the velocity estimate to remove noise. Again, the known physical dynamics of the vehicle can be used to produce a filter with almost no time delay, since the maximum propulsion force of the LSRM and thus the maximum vehicle acceleration (2.25 m/s^2) are limited. The velocity computation algorithm is implemented in a two-step process as follows.

$$\Delta v(n) = \frac{x_{ABS}(n) - x_{ABS}(n-1)}{\Delta T} - v(n-1)$$

$$v(n) = \begin{cases} \dfrac{x_{ABS}(n) - x_{ABS}(n-1)}{\Delta T} & \text{if } \left|\dfrac{\Delta vel(n)}{\Delta T}\right| < a_{\max} \\ vel(n-1) + a_{\max} \cdot \Delta T \cdot sign(\Delta vel(n)) & \text{otherwise} \end{cases} \quad (3.22)$$

Note that there are no maximum or minimum velocity restrictions with this approach—only the rate of change of velocity is limited. The result is that the velocity signal is filtered without time delay.

This algorithm is tested experimentally during open-loop operation of the position estimation system, as shown in Figure 9. Note that the LSRM is operating via the mechanical position transducer rather than sensorlessly, so the results have limited implications.

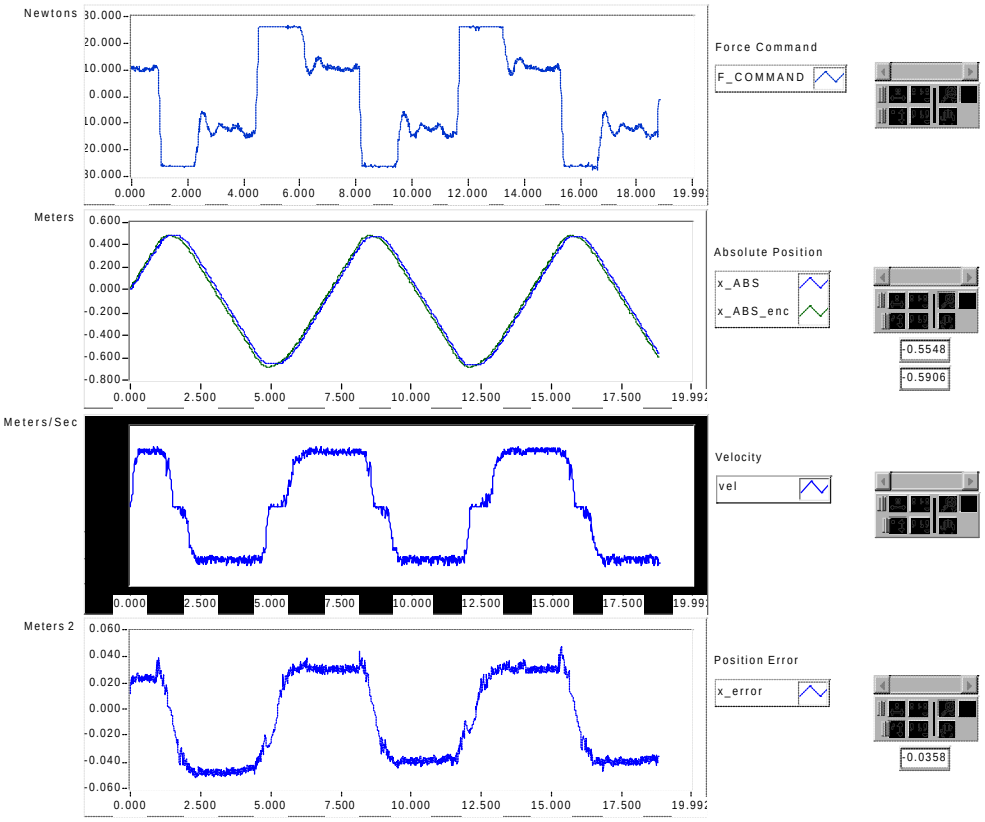

Figure 9. Open-loop Testing of the Proposed Position Algorithm

3.3 Inputs and Outputs of the Sensorless System

The sensorless position estimator is added to the LSRM system with the goal of minimizing the changes to the DSP control system and the amount of additional hardware, as in Figure 10. The estimator's data acquisition card probes the three existing analog signals from the phase winding current sensors. The phase voltage references are more difficult to obtain because they are not delivered from the DSP in analog form, but rather as a digital instruction word and sent to the interface board. Fortunately, the DSP has a configurable Digital to Analog Converter (DAC) subsystem that was originally intended to provide up to four internal values at analog outputs for diagnostic purposes. These DAC

channels are configured to output the force command and the voltage references for each phase. With these signals, the position estimator has sufficient information to estimate the flux linkages in each of the phases, and thus to estimate the relative position. However, the estimation of absolute position requires the knowledge of the initial position of the vehicle. This can be accomplished through the use of an index sensor, as was done by the position transducer; or by executing a start-up search procedure to locate the vehicle without a mechanical sensor by estimating its location from the phase inductance. During the development of the sensorless algorithm, the index sensor was initially used. The estimator processor is also used to implement closed loop control of the vehicle position via a Proportional (P) compensator. The compensator's output is a velocity command, which is transmitted to the DSP. The output of the position estimator is three Quadrature position signals, Q_A, Q_B, and Q_Z.

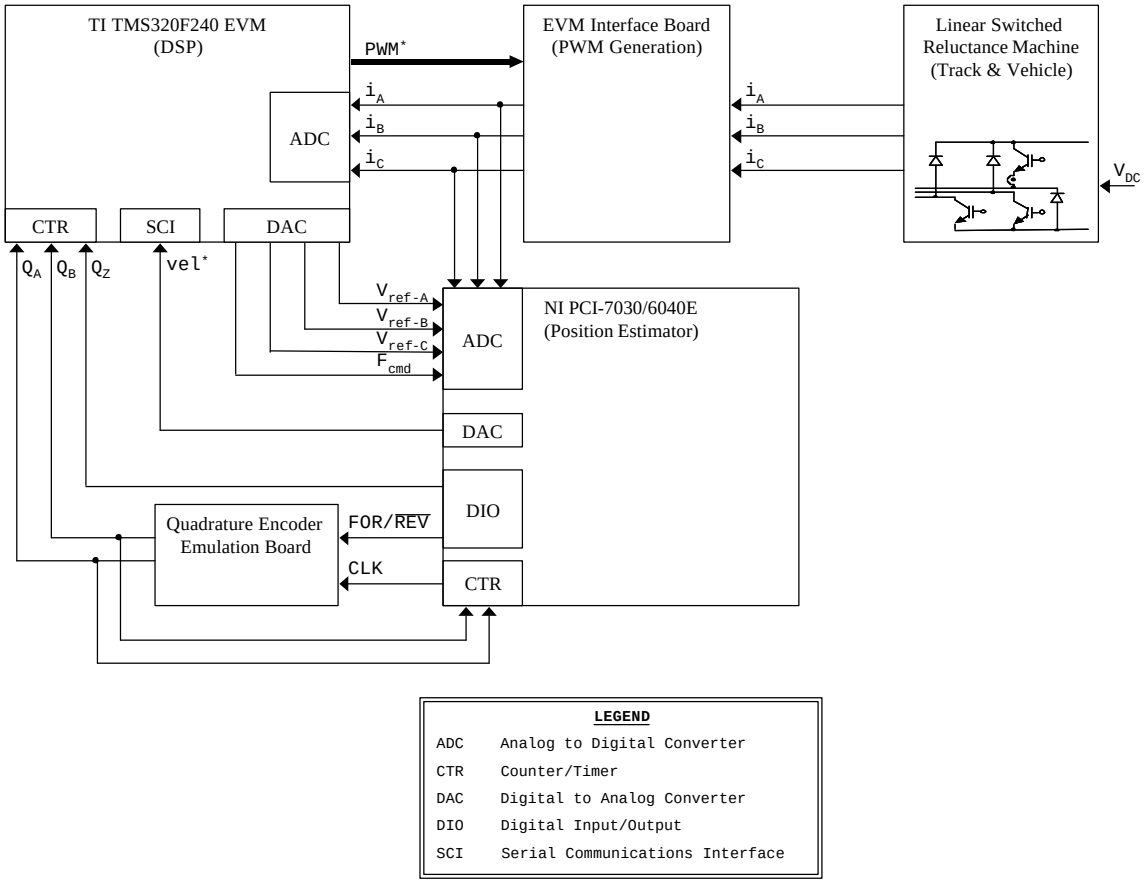

Figure 10. Inputs and Outputs of the Sensorless LSRM

3.3.1 Quadrature Position Encoder Emulation

The goal of the position encoder emulation subsystem is to mimic the output of a mechanical position transducer so the estimated position and velocity can be transmitted to the DSP without modifications to the DSP hardware or software. Quadrature encoding works by either incrementing or decrementing a counter on the DSP each time the vehicle travels a fixed incremental distance along the track, where X_{ABS} is the absolute position value stored in the DSP, $x(0)$ is the initial vehicle position where the Z-index reset sensor is located, CNT is the

counter value (an integer), and *RES* is the resolution of the position transducer in meters.

$$x_{ABS} = x(0) + CNT \cdot RES \tag{3.23}$$

The DSP counter is incremented or decremented and reset by three signals, Q_A, Q_B, and Q_Z. The first two are always 90 degrees out of phase, and one toggles state each time the vehicle moves *RESOLUTION* meters.

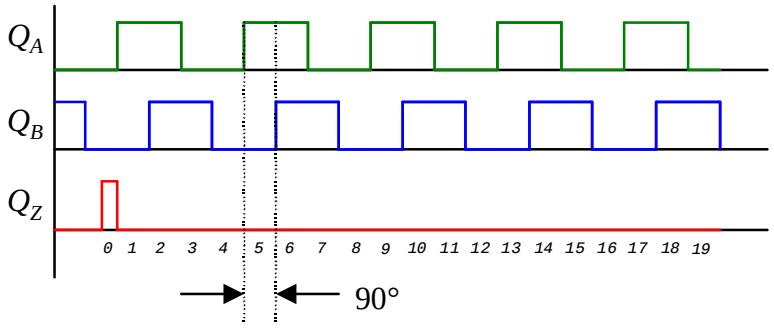

Figure 11. Quadrature Encoder Signals

If the vehicle is moving forward, the Q_A signal will toggle high when Q_B is low (Q_A leads). If the vehicle is moving backward, the Q_B signal will toggle high when Q_A is low (Q_B leads), as in Figure 12.

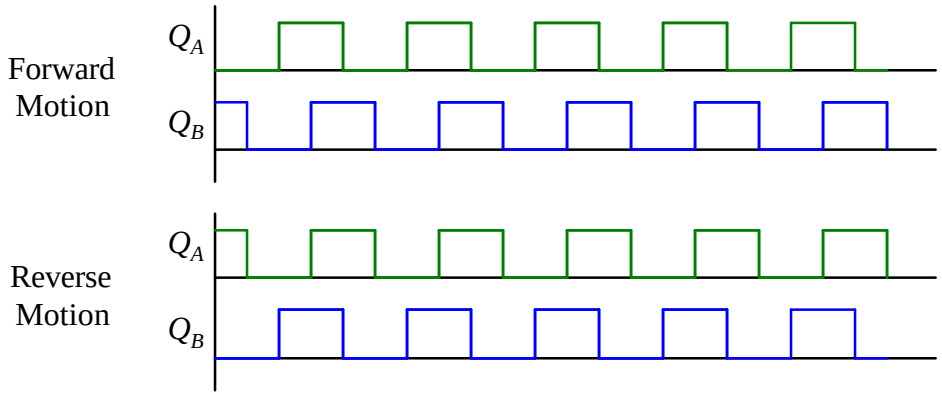

Figure 12. Forward and Reverse Motion
Quadrature Encoding

The Q_Z signal is used to initialize the DSP absolute position counter when the Z-index reset sensor passes its home location at start-up. The LabVIEW™ DAQ daughter card is equipped with two 24-bit counters. One is used to generate a clock pulse and the other is programmed to monitor the Q_A and Q_B signals generated by the emulator board.

3.3.2 Start-Up Search Procedure

A start-up search procedure is required if the initial location of the vehicle is not known. The procedure is used to estimate the location of the vehicle translator by measuring the inductance of each phase. This approach is favored over the use of a mechanical sensor, and it also eliminates the need to manually move the vehicle past the index sensor when the system is started, which requires human intervention. The search procedure uses the fact that the self-inductance of the phase windings depends on the proximity of the vehicle translator. If the translator is not in the vicinity of the energized phase winding, then the inductance will be close to some minimum value, L_{MIN}. If the inductance is larger, however, then the translator is in the proximity of that phase winding and the 2-D position Look Up Table can be used to estimate the position of the translator

relative to that phase winding. If the translator is in that proximity then the next five phases should also have inductances larger than L_{MIN}, so they can also be used to estimate the relative position of the vehicle. Then the average of the six relative position estimates can be computed and used to estimate the absolute position of the translator. Finally, the DSP position counter must be initialized to the estimated absolute position. Then, the sensorless LSRM may begin its normal operation.

This approach requires that each coil be energized until the vehicle translator is located. This is accomplished by initializing the DSP position counter and then using Quadrature encoder emulation to simulate the motion of the vehicle along the track. This "tricks" the DSP into energizing the track coils, which can then be used to estimate the phase inductance. The DSP is programmed to propel the vehicle back and forth between two locations on the track at a fixed speed of 0.4 m/s. Figure 6 shows the velocity loop and PI compensator internal to the DSP that are used to generate the force and current commands based on the vehicle speed error. The Quadrature encoder emulator can be used to set this error to a fixed value, such as 0.1 m/s, by generating a Quadrature position signal with a velocity of 0.3 m/s. This results in a bounded and nonzero current command, and the phase inductance can thus be determined and used to estimate position.

3.3.3 Operational Flow Chart

As in Figure 13, the sensorless algorithm begins its operation by initializing the hardware. This includes configuration of the various hardware subsystems such as the Analog to Digital Converter (ADC) and the counter/timers (CTR). The DSP is also initialized at this time, and the DC link is energized. Then a start up procedure takes place to initialize the vehicle location information stored in

the DSP counter. If a mechanical reset sensor is used, the vehicle must be manually moved over the sensor, which generates the Q_Z pulse. Alternately, a sensorless start-up procedure may be used to locate the vehicle using phase inductance data generated by scanning the track. First, an artificial Q_Z pulse is generated by the sensorless processor, a velocity command is generated, and each phase winding is excited so the maximum inductance of each phase can be measured and the phase with maximum inductance can be located. The estimator then computes the location of the vehicle and moves the position counter back to the appropriate location. At this point, the LSRM may begin normal operation and the sensorless estimation algorithm begins estimating and updating the DSP position counter continuously.

The algorithm begins each iteration by acquiring the phase currents, phase voltage references, and the force command. These signals are scaled to their appropriate magnitudes by the data acquisition hardware. Then the flux linkage in each phase is updated by integrating the phase voltages and currents, according to Equation 3.19. Although only one phase is used to estimate position at a time, the flux linkage calculation must be run for all three phases since the integration operation is a continuous process. The optimal phase for position and velocity estimation is then selected, and the 2-D position Look Up Table is used to estimate the relative position using the flux linkage and current values of the optimal phase. Finally, the absolute position of the translator is calculated based on the change in relative position and the position encoder counter is updated to produce the appropriate values for position and velocity at the DSP position counter.

Figure 13 also shows the sources of error in the algorithm. In the following chapter, these sources of error and their propagation through the estimator will be studied in detail.

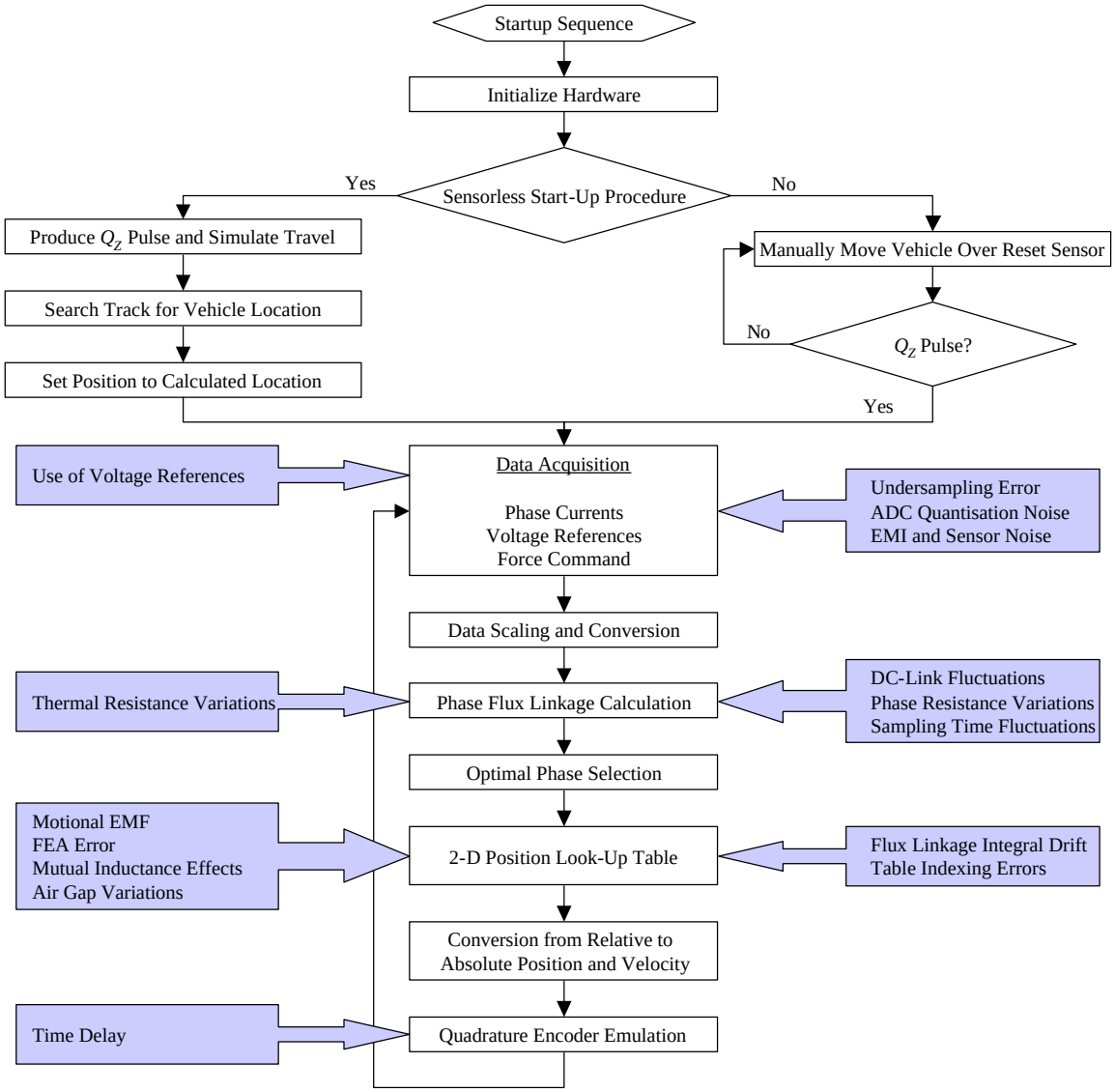

Figure 13. Operational Flowchart for Proposed Sensorless Algorithm with Error Sources

Chapter 4

SOURCES AND PROPAGATION OF ERROR

4.1 Background Information

Position estimation error is a problem inherent to any Switched Reluctance Machine, with or without a mechanical position transducer. The resolution and accuracy of the measured or estimated position information often dictates an upper limit on the quality and performance of the control system, including its efficiency and smoothness. For low-grade control applications such as fans and pumps, SRMs often use optical encoders that give absolute position updates every 10 to 20 electrical degrees. Real time interpolation based on the estimated velocity can be used to give the controller improved resolution for precise commutation. Higher performance applications often use hall sensors or R/D converters to achieve resolutions of less than one electrical degree.

The resolution and accuracy of the sensorless estimation schemes proposed in literature may vary widely. The comparison of one scheme to another is complicated by the fact that the performance of each sensorless implementation depends to a large extend on the design of the machine, its converter, and controller. Sensorless performance may also vary significantly over the speed and load operating range of the machine. Some approaches perform best at low speed, while others perform best under high loading conditions. The machine design determines the position sensitivity and influences the performance of a sensorless scheme, particularly the ratio of aligned and unaligned inductances. Start-up performance for hesitation-free starting can also vary significantly among the techniques, and self-starting is not possible with some approaches.

It seems reasonable that a sensorless position estimator might have its performance characterized in a manner akin to that for a mechanical position transducer. Common performance characteristics include; (a) resolution, or the smallest change in position that can be reliably detected, (b) accuracy, or the certainty of the output relative to the true position, (c) drift, or the shift in output in one direction due to miscalibration or temperature effects, and (d) linearity, or the consistency of the response over the range of operation.

The goal of the sensorless designer is to produce a position estimator that is comparable in performance to a mechanical position transducer. In addition, the cost and complexity of the scheme must be minimized. Difficult trade-offs must be made when considering factors such as, (a) the required performance at start-up and over the entire operational range of the machine, (b) the complexity of the sensorless scheme, (c) the number of inputs, (d) the amount of additional hardware, (e) the computational expense, processor time, and memory requirements.

A few investigators have addressed the issue of error analysis in sensorless position estimation, as in [43, 49, 51, 57, 58]. This chapter presents a systematic analysis of the sources and propagation of error through the hardware and software of the SRM and sensorless estimator using statistical techniques based on a combination of analytical and experimental results. The goal is to gain insight into the sources of error in the sensorless system, to systematically trace its propagation, and to derive some useful insight. The results are not intended to be an exact specification of the estimation error in the machine. While adherence to principals of statistical error analysis is sought, assumptions are sometimes made to simplify and expedite the process. Likewise, it is not possible to include all sources of error in the analysis but it is hoped that a representative sample of the most important sources is considered. The analysis that follows is most useful as

a way to ascertain the validity of the proposed algorithms from an error perspective and to determine which sources of error are most troublesome and thereby make the best candidates for error mitigation efforts.

4.2 Sources of Error

The sources of error for the sensorless position estimator can be broadly categorized as resulting from, (a) unmodeled physical phenomena, and (b) measurement and computational inaccuracies. Figure 13 shows the types of error that will be considered in this analysis, with the first category of error on the left and the second on the right. Before beginning the analysis, each type of error will be briefly introduced.

4.2.1 Unmodeled Physical Phenomenon

Unmodeled physical phenomena are the most difficult error sources to quantify. These exist in part because some of the more complicated dynamics of the LSRM must be ignored to make the sensorless scheme simple enough for real-time implementation for practical implementation at operational speeds. Some physical dynamics are not modeled because to do so would either require more inputs (such as an air gap sensor), or would be computationally intensive. In the proposed implementation, motional emf effects at higher speeds and the mutual coupling between adjacent phases are examples of unmodeled machine dynamics. Sources of error in this category include the effects of using the voltage reference (duty cycle command) signal rather than the measured phase voltage, error from Finite Element Analysis (FEA) calculations of the magnetic properties, and air gap variations.

4.2.2 Measurement and Computational Errors

Measurement and computational errors are specific to the hardware and software of the sensorless estimator. Fortunately, this type of error is generally random in nature and its analysis can usually be facilitated via statistical analysis of experimental data. Standard deviation (RMS value), and expected value (mean) are the most commonly used statistical quantities. The sources of error under scrutiny in this category include undersampling error, quantisation noise, EMI noise, DC-link voltage fluctuations, resistance variations, sampling time variations, flux linkage integral drift, position table indexing, and error from the conversion between relative and absolute position.

4.3 Propagation of Error

To arrive at an estimate of the total position uncertainty at the output of the position estimation system, each probable source of error is traced through the hardware and software of the sensorless system. The principal benefit of this process is in developing a good understanding of the error and the relative importance of each source. It should be noted that the error sources may be summed quadratically if they are random and independent. Otherwise, the error sources sum through direct addition. The quadratic sum tends to exaggerate the terms with the largest magnitudes and tends to make the smaller terms less significant. The result of quadratic addition is that smaller sources of error tend to have little effect on the position uncertainty while others tend to dominate. The total uncertainty in a function of several variables is given in the following theorem adapted from Taylor [**58**].

Uncertainty in a Function of Several Variables

Suppose x,…, z are values measured with uncertainties dx,…, dz, and the measured values are used to compute the function g(x,…,

z). If the uncertainties in x,…,z are independent and random, then the uncertainty in q is

$$dg = \sqrt{\left(\frac{\partial g}{\partial x}\,dx\right)^2 + \ldots + \left(\frac{\partial g}{\partial z}\,dz\right)^2}. \qquad (4.24)$$

The uncertainty is always less than the ordinary sum

$$dg \le \left|\frac{\partial g}{\partial x}\right| dx + \ldots + \left|\frac{\partial g}{\partial z}\right| dz. \qquad (4.25)$$

The position estimate is achieved in three distinct steps using the flux/voltage method proposed in this study. First, the required physical quantities of interest (the phase currents and voltage references) are measured directly. Then Faraday's Law is used to calculate the flux linkage using the trapezoidal integration form of Equation 3.19. Finally, the calculated flux linkage is used to estimate position through the use of a 2-Dimensional Look Up Table. In Chapter 3, the operational flowchart for the algorithm was explained in more detail.

The error analysis process to find the position uncertainty involves multiple steps. First, the uncertainty of the variables in the flux linkage equation is estimated. Then Equation 4.24 is evaluated to find the total flux linkage calculation uncertainty. The result is used to estimate the random position uncertainty at the output of the position Look Up Table. In addition, the sources of systematic error from unmodeled physical dynamics are considered.

4.3.1 Random Flux Linkage Calculation Errors

The first step in the random error analysis process is to develop an estimate for the uncertainty of each variable in the numerical flux linkage equation. This equation is repeated again for convenience.

$$\begin{aligned} l_k(0) &= 0 \\ l_k(n) &= l_k(n-1) + \\ &\frac{\Delta T}{2}\left(V_{DC} \cdot v_{ref-k}(n) + V_{DC} \cdot v_{ref-k}(n-1) - R \cdot i_k(n) - R \cdot i_k(n-1)\right) \end{aligned} \tag{4.26}$$

In some cases, such as quantisation noise in the voltage and current measurements, the uncertainty can be determined from well-known formulas. In other cases, the uncertainty can be estimated from statistical experimental data, such as the standard deviation of the DC-link voltage. Several variables, namely *?(n-1)*, v_{ref}*(n-1)*, and *i(n-1)*, presumably have no uncertainty since they are simply stored in computer memory from one iteration to the next.

4.3.1.1 Error from Undersampling

Due to the fact that the sensorless data acquisition system samples the phase voltages and currents at a frequency much less than the Nyquist rate, we anticipate that some of the information contained in the analog voltage reference and current signals will be lost. Under ideal circumstances, the voltages and currents in the phase windings might be sampled at two times the switching frequency, or 20,000 Samples/Second. Due to the time required to complete each computation, the sensorless estimator sampling frequency, f_s, is only 10,000 Samples/Second.

It is proposed that this error can be estimated through experimental measurements of the operational voltage and current waveforms using a fast

sampling rate of 100,000 Samples/Second. The waveform acquired at the high sampling rate is considered the true waveform, $i(t)$. Then the standard deviation of the difference between the true waveform and the undersampled waveform, $\tilde{i}(t)$, can be calculated and used to estimate the RMS uncertainty due to undersampling in each acquisition, di_s. Note that the uncertainty calculation converges as data set increases in length. A straight line is draw between each undersampled waveform so that the error mimics trapezoidal integration. This is illustrated graphically for an example waveform in Figure 14.

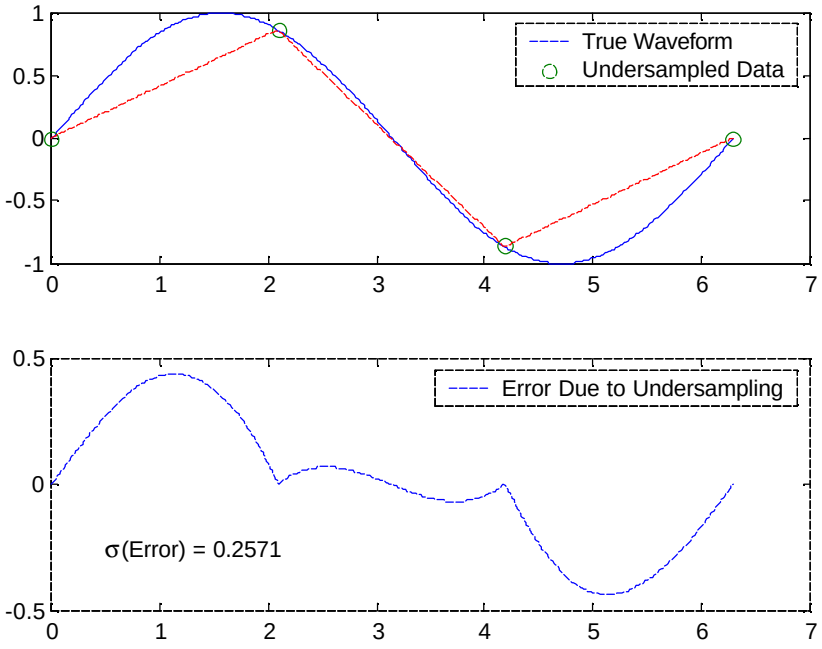

Figure 14. Example Illustrating the Calculation of Undersampling Error

Using this method, the voltage reference and current uncertainties are estimated using experimental data. This analysis uses one second of experimental data collected at 100,000 samples per second.

$$dv_{ref-s} = s\left(v_{ref}(t) - \tilde{v}_{ref}(t)\right) = 23.0 \times 10^{-3} \text{ Units/Sample}$$
$$di_s = s\left(i(t) - \tilde{i}(t)\right) = 79.4 \times 10^{-3} \text{ A/Sample} \quad (4.27)$$

4.3.1.2 Error from Quantisation Noise

Quantisation noise is another source of error that originates in the Analog to Digital Converter (ADC). The data acquisition system is a high performance PCI-6040E daughter card by National Instruments featuring 12-bit word length and ±0.5 LSB accuracy. The system reads the analog voltage reference signals produced by the DSP and the phase current sensor values on a 0 to 5 V scale, resulting in a resolution of 1.2 mV.

The Root Mean Square (RMS) quantisation noise from this acquisition system is expressed in Equation 4.28, where $dv_{ref\text{-}ADC}$ is the RMS voltage reference error per acquisition due to quantisation, and di_{ADC} is the RMS phase current quantisation error per acquisition, n is the word length in bits of the analog to digital converter (12 bits), $v_{ref\text{-}MAX}$ is the range of the voltage reference command (2 Units), and I_{MAX} is the maximum value of the phase current sensor reading (10 Amps) [57].

$$dv_{ref-ADC} \approx 0.294 \cdot 2^{-2n} \cdot v_{ref-MAX} = 0.294 \cdot 2^{-2 \cdot 12} \cdot 2 = 35.0 \times 10^{-9} \text{ Units/Sample}$$
$$di_{\text{ADC}} \approx 0.294 \cdot 2^{-2n} \cdot I_{MAX} = 0.294 \cdot 2^{-2 \cdot 12} \cdot 10 = 175.2 \times 10^{-9} \text{ A/Sample} \quad (4.28)$$

4.3.1.3 Error from Electromagnetic Interference (EMI) and Sensor Noise

The corruption of measured signals due to Electromagnetic Interference (EMI) and sensor noise is a common problem in any real-world implementations involving data acquisition. The causes and treatment of EMI noise is beyond the

scope of this discussion. Instead, it is intended only to roughly characterize the RMS value of the error introduced by EMI through experimental statistics. This is accomplished by computing the standard deviation of a static signal acquired at the normal sampling rate while the machine is in operation at 0.4 m/s. From these experimental measurements, the uncertainty in the measured values due to EMI is estimated as follows.

$$\begin{aligned} dv_{ref-EMI} &= 1.88 \times 10^{-3} \text{ Units/Sample} \\ di_{EMI} &= 10.1 \times 10^{-3} \text{ A/Sample} \end{aligned} \tag{4.29}$$

4.3.1.4 Error from DC-Link Voltage Fluctuations

Another source of error comes from the fluctuations in the DC-link voltage due to the transient current drain on the bus from coil excitations during normal operations. An estimate for the RMS value of this error for a single acquisition is obtained from experimental measurements of the DC-link voltage fluctuation. The standard deviation (equivalent to RMS value) of the DC-link voltage is measured using a built in function of a digital oscilloscope while the LSRM vehicle is operating at 0.4 m/s.

$$dV_{DC} \approx s\,(V_{DC}) = 1 \text{ V/Sample} \tag{4.30}$$

4.3.1.5 Error from Phase-to-Phase Winding Resistance Variations

It is also known that fluctuations in the phase winding resistance will result in an error in the assumed phase resistance. This error is assumed to come from the resistance differences among the 120 individual stator windings on the track. For error modeling purposes, this error is treated as stochastic in nature. An estimate for this error is achieved by measuring the LSRM winding resistances using a digital multimeter, and computing the standard deviation via spreadsheet

analysis. The vehicle is again assumed to be operating at 0.4 m/s. The uncertainty in the winding resistance during travel is approximated by Equation 4.31, where and $s(R)$ is the standard deviation of the experimentally measured winding resistances, w_{st} refers to the spacing between the stator poles (40 mm), and vel is the vehicle velocity (0.4 m/s).

$$dR \approx \frac{s(R)}{f_s}\frac{vel}{w_{st}} = \frac{0.0504}{10{,}000}\frac{0.4}{0.04} = 50.4 \times 10^{-6}\ \Omega/\text{Sample} \tag{4.31}$$

4.3.1.6 Error from Temperature Dependent Resistance Variations

Temperature variations resulting in resistance changes are not considered in this random error propagation analysis, because their rate of change is so small that the error induced in a single sampling is assumed to be negligible. Another reason for neglecting temperature related resistance variations stems from the nature of the linear machine. Unlike rotary machines, the phase winding duty cycle is very low in the LSRM because only the phases adjacent to the vehicle are excited during operation. Thus, the temperature variations are expected to be less important than in a rotary machine. Resistance changes due to temperature variation are grouped in the *systematic error* category. In other words, the temperature related resistance change will result in a static error in the flux linkage calculation; causing it to be consistently too large or too small. Systematic errors such as this are akin to the miscalibration of a measuring device, and they are not included in the uncertainty equation. The presence of systematic error suggests that a calibration of the sensorless algorithm may be required.

4.3.1.7 Error from Sampling Time Fluctuations

This source of error stems from the fact that the data acquisition sampling time is used in the flux linkage calculation. This sampling time is configured via

software before the algorithm begins, and the data acquisition system uses a hardware counter to achieve the desired sampling interval. The analog to digital converter performs conversions on each channel asynchronously, so there is also an interchannel delay between samples acquired on different channels. Information from the manufacturer indicates that sampling time fluctuations are on the order of nanoseconds for the chosen hardware. The interchannel delay (about 14 microseconds) is fairly consistent from one acquisition to the next since the channels are sampled in the same order, so this is not considered a source of random error in the analysis. Thus, the interchannel delay is neglected and the sampling time fluctuation is given as follows.

$$d\Delta T \approx s(\Delta T) = 1 \times 10^{-9} \text{ s/Sample} \tag{4.32}$$

4.3.1.8 The Total Uncertainty of Each Variable

The total uncertainty of each variable can be computed through Quadrature addition since each source contributing to the same variable is modeled as if it were independent and random in nature.

$$\begin{aligned}
&dv_{ref} = \sqrt{(dv_{ref-s})^2 + (dv_{ref-q})^2 + (dv_{ref-EMI})^2} = \\
&19.3 \times 10^{-3} \text{ Units/Sample} \\
&di = \sqrt{(di_s)^2 + (di_q)^2 + (di_{EMI})^2} = \\
&80.0 \times 10^{-3} \text{ A/Sample} \\
&dV_{DC} = 1 \text{ V/Sample} \\
&dR = 50.4 \times 10^{-6} \ \Omega\text{/Sample} \\
&d\Delta T = 1 \times 10^{-9} \text{ s/Sample}
\end{aligned} \tag{4.33}$$

4.3.1.9 The Relative Magnitude of Each Variable

Since the form of the uncertainty formula given by Equation **4.24** distinguishes the error contribution from each error variable, it is possible to compare the magnitude of each source relative to one another. The interpretation is complicated by the fact that the sources sum in quadrature, since the larger error sources tend to dominate. Nonetheless, some insight might be gained by plotting the relative magnitudes of each error sources, as in Figure 15. It can be seen that voltage reference uncertainties are the primary source of error, while sampling time fluctuations and resistance variations are relatively unimportant. In the case of the voltage reference uncertainty, undersampling is the greatest source of random error. Phase current uncertainties and DC-Link voltage fluctuations are the other principal sources. Note that this analysis does not include systematic error, which is discussed subsequently.

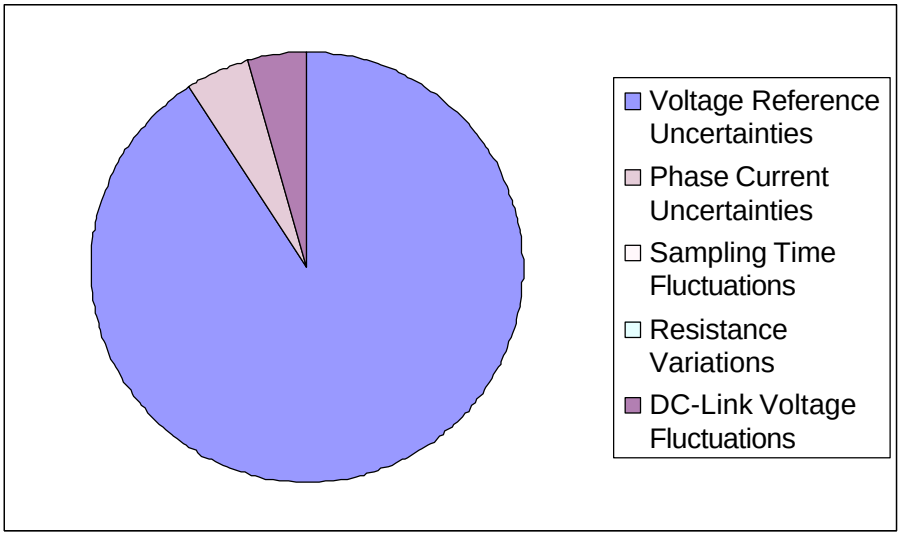

Figure 15. Relative Magnitude of Each Random Error Variable in the Flux Linkage Calculation (Systematic Error Not Included)

4.3.2 The Total Random Flux Linkage Calculation Uncertainty

Taking into account all the error sources described above, the numerical flux linkage equation (Equation 4.26) can be rewritten as follows.

$$
\begin{aligned}
& l_c(0) = 0 \\
& l_c(n) = l(n-1) + \\
& \frac{(\Delta T + d\Delta T)}{2}\left(\begin{array}{l} (V_{DC} \pm dV_{DC})(v_{ref}(n) \pm dv_{ref} + v_{ref}(n-1)) - \\ (R \pm dR)(i(n) \pm di + i(n-1)) \end{array} \right)
\end{aligned}
\qquad (4.34)
$$

Assuming that the error variables are independent and random, we can use Equation **4.24** to find the total uncertainty in each iteration of the flux linkage estimate. This yields the flux linkage uncertainty per calculation as in Equation **4.35**. The overbar notation, as in $\overline{V}_{DC}$, is used to denote the expected or mean

value of the quantity. These are obtained from statistical analysis of experimental data with the vehicle operating at 0.4 m/s.

$$
\begin{aligned}
dl_c &= \sqrt{\left(\frac{\partial l}{\partial \Delta T}\,d\Delta T\right)^2 + \left(\frac{\partial l}{\partial V_{DC}}\,dV_{DC}\right)^2 + \left(\frac{\partial l}{\partial v_{ref}}\,dv_{ref}\right)^2 + \left(\frac{\partial l}{\partial R}\,dR\right)^2 + \left(\frac{\partial l}{\partial i}\,di\right)^2} \\
\frac{\partial l}{\partial \Delta T}\,d\Delta T &= -\frac{d\Delta T}{2}\left[\begin{array}{l}\overline{R}\left(\bar{i}(n) + \bar{i}(n-1)\right) + \\ \overline{V}_{DC}\left(\bar{v}_{ref}(n) + \bar{v}_{ref}(n-1)\right)\end{array}\right] \\
\frac{\partial l}{\partial V_{DC}}\,dV_{DC} &= \frac{dV_{DC}\cdot\Delta\overline{T}}{2}\left(\bar{v}_{ref}(n) + \bar{v}_{ref}(n-1)\right) \\
\frac{\partial l}{\partial v_{ref}}\,dv_{ref} &= \frac{dv_{ref}\cdot\Delta\overline{T}}{2}\,\overline{V}_{DC} \\
\frac{\partial l}{\partial R}\,dR &= -\frac{dR\cdot\Delta\overline{T}}{2}\left(\bar{i}(n) + \bar{i}(n-1)\right) \\
\frac{\partial l}{\partial i}\,di &= -\frac{di\cdot\Delta\overline{T}}{2}\,\overline{R}
\end{aligned}
\tag{4.35}
$$

Because the expected value of the voltage reference and current are constant, the uncertainty equations can be rewritten as follows.

Let $\bar{i}(n) = \bar{i}(n-1) = \bar{\bar{i}}, \bar{v}_{ref}(n) = \bar{v}_{ref}(n-1) = \bar{\bar{v}}_{ref}$

Then,

$$\frac{\partial l}{\partial \Delta T} d\Delta T = d\Delta T\left(\bar{\bar{R}} \cdot \bar{\bar{i}} + \bar{\bar{V}}_{DC} \cdot \bar{\bar{v}}_{ref}\right)$$

$$\frac{\partial l}{\partial V_{DC}} dV_{DC} = dV_{DC} \cdot \Delta\bar{\bar{T}} \cdot \bar{\bar{v}}_{ref} \tag{4.36}$$

$$\frac{\partial l}{\partial v_{ref}} dv_{ref} = dv_{ref} \frac{\bar{\bar{V}}_{DC} \cdot \Delta\bar{\bar{T}}}{2}$$

$$\frac{\partial l}{\partial R} dR = dR \cdot \Delta\bar{\bar{T}} \cdot \bar{\bar{i}}$$

$$\frac{\partial l}{\partial i} di = di \frac{\bar{\bar{R}} \cdot \Delta\bar{\bar{T}}}{2}$$

Representative magnitudes for the expected value of each variable are obtained from experimental data while the prototype operates at 0.4 m/s. These are listed below.

$$\begin{aligned}
\bar{\bar{i}} &= 2.45 \text{ A} \\
\bar{\bar{v}}_{ref} &= 19.3 \times 10^{-3} \text{ Units} \\
\Delta\bar{\bar{T}} &= 100 \times 10^{-6} \text{ s} \\
\bar{\bar{R}} &= 1.258\ \Omega \\
\bar{\bar{V}}_{DC} &= 80 \text{ V}
\end{aligned} \tag{4.37}$$

The total random flux linkage calculation uncertainty is thus given by Equation **4.38**.

$$dl_c = \sqrt{\left(\frac{\partial l}{\partial \Delta T}\, d\Delta T\right)^2 + \left(\frac{\partial l}{\partial V_{DC}}\, dV_{DC}\right)^2 + \left(\frac{\partial l}{\partial v_{ref}}\, dv_{ref}\right)^2 + \left(\frac{\partial l}{\partial R}\, dR\right)^2 + \left(\frac{\partial l}{\partial i}\, di\right)^2} =$$

$$\sqrt{\left[d\Delta T\left(\overline{R}\cdot\bar{i} + \overline{V}_{DC}\cdot\bar{v}_{ref}\right)\right]^2 + \left[dV_{DC}\cdot\Delta\overline{T}\cdot\bar{v}_{ref}\right]^2 + \left[dv_{ref}\,\frac{\overline{V}_{DC}\cdot\Delta\overline{T}}{2}\right]^2 + \left[dR\cdot\Delta\overline{T}\cdot\bar{i}\right]^2 + \left[di\,\frac{\Delta\overline{T}}{2}\right]^2} = \quad (4.38)$$

$77.4 \times 10^{-6}\ \mathrm{V}\cdot\mathrm{s/Sample}$

4.3.2.1 Drift in the Flux Linkage Calculation

The error involved in each computation builds over time in the flux linkage calculation until the integrator is reset, and is thus a function of time. The uncertainty in each iteration is assumed to be random and independent, and thus it builds through quadratic addition rather than through direction addition. The cumulative effect of integrator drift over time can then be expressed as follows, where t_r is the time in seconds when the integrator was last reset, and t is the time variable.

$$\sum dl_c(t) = \sqrt{f_s \cdot (t - t_r) \cdot (dl_c)^2} \quad (4.39)$$

We would expect this integrator error, or drift, to be more problematic at low speeds due to the increased time between resets. Because the commutation behavior of the DSP based controller is determined by the Force Distribution Function, we can write the expected time between resets in terms of the vehicle velocity as follows, where w_{comm} is the length of track over which we expect a non-zero phase current, or 30 mm in the prototype LSRM.

$$\left(t - t_r\right) = \frac{w_{comm}}{vel} \tag{4.40}$$

Just before the reset occurs, the integrator drift will be maximum, so Equation **4.40** can be substituted into **4.39** to obtain the maximum integrator drift as a function of velocity. This is plotted in Figure 16 for the LSRM.

$$\sum dl_{c-MAX}(vel) = \sqrt{f_s \cdot \frac{w_{comm}}{vel} \cdot \left(dl_c\right)^2} \tag{4.41}$$

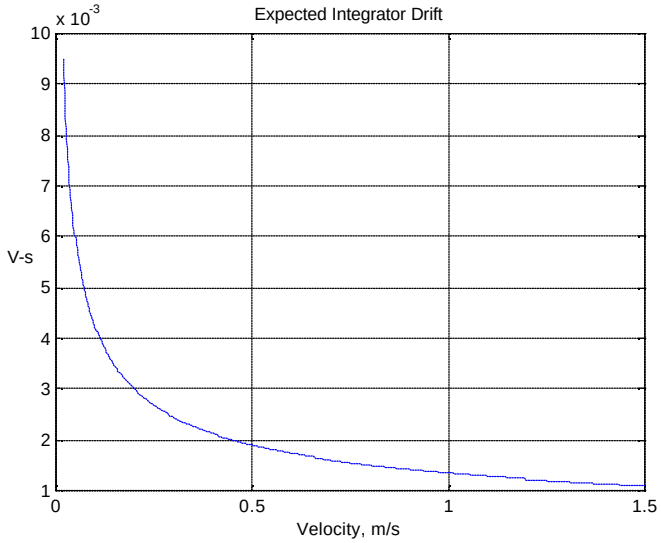

Figure 16. Expected Integrator Drift as a Function of Velocity

4.3.2.2 Position Table Indexing Errors

The position look up table uses the calculated flux linkage and acquired phase current as inputs. The table is a 121 by 121 array of single precision numbers where each row corresponds to one value of flux linkage and each column corresponds to one value of phase current, and each value in the table corresponds to a position in the first half of the translator cycle. Since the range

of flux linkage for the machine is 0 to 0.31 V-s, the flux linkage resolution of the table is 2.64 x 10^{-3} V-s. Likewise, the range of currents for the machine is 0 to 10 Amps, so the current resolution of the table is 82.6 x 10^{-3} Amps.

Because the indexing of the table requires integer inputs, the flux linkage and phase current values are first multiplied by a scaling factor and then converted to integer format for indexing. In the process, the values are rounded upwards or downwards according to IEEE standards. This rounding action results in a truncation error, which if assumed to be random will have a Gaussian distribution and can be treated similarly to quantisation noise. The dimensions of the table, however, are not powers of two so the next lowest integer is used. Thus, the table dimensions are approximated as 2^7 by 2^7, or 128 by 128.

$$\begin{aligned} d\,l_{ind} &\approx 0.294 \cdot 2^{-2n} \cdot l_{MAX} = 0.294 \cdot 2^{-2 \cdot 7} \cdot 0.32 = \\ & 5.74 \times 10^{-6}\ \text{V} \cdot \text{s/Sample} \\ d\text{i}_{ind} &\approx 0.294 \cdot 2^{-2n} \cdot I_{MAX} = 0.294 \cdot 2^{-2 \cdot 4} \cdot 10 = \\ & 179.4 \times 10^{-6}\ \text{A/Sample} \end{aligned} \tag{4.42}$$

4.3.2.3 Total Random Uncertainty in the LUT Inputs

Each source of random error in the variables of the flux linkage integral have been quantified individually and can be used to compute the total flux linkage calculation uncertainty. This is combined with the position table indexing error via quadrature addition to arrive at a value for the total uncertainty in the position Look Up Table (LUT) Inputs. It can be seen that air gap variations are the predominant source of error and that flux linkage calculation error and position table indexing error have a negligible effect.

$$
\begin{aligned}
&d\lambda_{rand} = \sqrt{(d\lambda_c)^2 + (d\lambda_{ind})^2} = \\
&\sqrt{\left(77.4 \times 10^{-6}\right)^2 + \left(5.74 \times 10^{-6}\right)^2} = \\
&77.6 \times 10^{-6} \text{ V} \cdot \text{S/Sample} \\
&di_{rand} = \sqrt{(di)^2 + (di_{ind})^2} = \\
&\sqrt{\left(80.0 \times 10^{-3}\right)^2 + \left(179.4 \times 10^{-6}\right)^2} = \\
&80.0 \times 10^{-3} \text{ A/Sample}
\end{aligned}
\tag{4.43}
$$

4.3.2.4 Total Random Uncertainty in the LUT Output

Now that an estimate for the total random error has been developed, the next task is to quantify the effect on the uncertainty at the position output of the Look Up Table. The magnetic sensitivity of the phase inductance with respect to position is used to provide the translation between flux linkage and position uncertainty. The magnetic sensitivity, detailed in Section 4.3.3.4, is used to map the uncertainty in flux and current at the table inputs to position uncertainty at the output. This is accomplished by first converting the flux linkage uncertainty to inductance by dividing by the expected value of the current. For the phase current input to the table, Equation 3.10 is first differentiated by current so the flux linkage uncertainty can be written as a function of current uncertainty. The uncertainty caused by the flux linkage and current are assumed to be random and independent, so the total uncertainty at the Look Up table output is given as follows.

$$
\begin{aligned}
&dx_{LUT} \approx \sqrt{\left[\frac{d\lambda_{rand}}{\bar{i}} \cdot \frac{\partial L}{\partial x}\right]^2 + \left[di_{rand} \cdot \frac{\bar{\lambda}}{\bar{i}^2} \frac{\partial L}{\partial x}\right]^2} = \\
&\sqrt{\left[\frac{77.6 \times 10^{-6}}{2.45} \cdot 1.25\right]^2 + \left[80.0 \times 10^{-3} \cdot \frac{0.1}{(2.45)^2} \cdot 1.25\right]^2} = \\
&2.51 \times 10^{-3} \text{ m/Index}
\end{aligned}
\tag{4.44}
$$

4.3.2.5 Conversion from Relative to Absolute Position

As described in Chapter 3, the position estimate generated by the LUT must be first converted to relative position via Equation **3.17**, and then to absolute position via Equation **3.21**. In the first case, it assumed that no error is introduced by the conversion from the LUT position to the relative position. This is because Equation **3.17** involves only internally stored variables. However, the conversion from relative to absolute position is likely to involve error that builds over time and causes the absolute position to diverge. Under these assumptions, this source of error correlates with the build up of error in the flux linkage integration, as previously described.

4.3.3 Systematic Error and Unmodeled Physical Phenomenon

In this section, a number of error sources from unmodeled physical phenomenon are considered. These error sources are systematic in nature rather than random. If we were to take a large number of position estimations and compute the average, the random error could be reduced. The same is not true for systematic errors, however. For instance, if the scaling of the flux linkage during position table Look Up is incorrect then all results will tend to be shifted in one direction. This type of error is perhaps the most difficult to detect and correct, but may have a significant effect on the accuracy of the estimator. The use of a measuring device with greater precision than the sensorless system is the most useful tool in detecting and analyzing systematic error. In this study, systematic and random error sources are treated separately and not combined.

4.3.3.1 Use of the Voltage Reference Signal Rather than Measured Voltage

Due to the large number of phase windings in the linear machine, it was decided not to measure the phase voltage directly through the addition of one

voltage sensor per coil. Instead, the voltage reference signal from the DSP controller (PWM duty cycle command) is measured by the sensorless system. If the interface board and unipolar converter are working properly, the average value of phase voltage over one switching cycle should be proportional to the voltage reference signal. In practice, we would expect that the true phase voltage would be different due to motional emf effects even if the converter were working ideally. Since the voltage reference is used in this implementation rather than the true phase voltage, motional emf effects are *not* expected to be a significant source of error. The magnitude of the motional emf is proportional to speed and can be computed as follows.

$$e = i \cdot vel \cdot \frac{\partial L}{\partial x} \tag{4.45}$$

4.3.3.2 FEA Error

The proposed sensorless scheme is essentially a flux/current method that uses the self-voltage in active phases. The flux linkage is calculated from measured signals and mapped to position. A 2-dimensional Look Up Table generated by Finite Element Analysis (FEA) is then used to perform the non-linear mapping function from flux linkage and current back to position. Although magnetic saturation effects in the magnetic circuit are included, several other magnetic effects are not, such as hysteresis, skin effects, eddy current losses, motional emf, and mutual-coupling between adjacent phases. While it is not necessarily difficult to include these effects using FEA software, their inclusion in the algorithm would certainly increase its complexity. Another simplification is made by including only half the translator cycle in the position Look Up Table, since the other half is assumed to be symmetrical about the aligned position.

The FEA computation itself also has uncertainty associated with it, since the numerical analysis software has limited accuracy. The magnitude of the uncertainty of the flux linkage data produced by the FEA software is difficult to quantify. For the purpose of this analysis the uncertainty of the FEA calculations is assumed to be about 7 percent. For simplicity, this error source is modeled as a systematic uncertainty in the flux linkage input to the position Look Up table.

$$d\lambda_{FEA} \approx 0.07 \cdot \bar{\lambda} = 0.07 \cdot 0.10 = 7.0 \times 10^{-3} \text{ V} \cdot \text{s} \tag{4.46}$$

4.3.3.3 Mutual Inductance Effects

Due to multiphase excitation, a more correct model for the phase inductance would be Equation 4.47, where M_{kj} is the mutual inductance between phase k and adjacent phase j, and M_{kl} is the mutual inductance between phase k and adjacent phase l.

$$\lambda_k = L_k i_k + M_{kj} i_j + M_{kl} i_l \tag{4.47}$$

In [50], J.P. Lyons, et. al. developed a flux/current sensorless algorithm that includes mutual inductance effects via a lumped parameter model. However, the algorithm was computationally intensive and had to be accomplished off-line. Mutual inductance effects are ignored in this implementation to preserve the speed efficiency of the algorithm.

4.3.3.4 Magnetic Sensitivity

An important observation regarding the mapping of magnetic properties to position has to do with the position sensitivity of the property, or how much the inductance/flux linkage changes with respect to position. It has been observed in literature that the sensitivity of estimation in an SRM is related to the ratio of the

aligned and unaligned inductances and the topology of the machine. The LSRM used in this study is a three-phase, 6/4 topology machine with an inductance ratio of 5.

In this study it is proposed that the sensitivity can be approximated as the absolute value of the change in phase inductance with respect to position, $\left|\partial L_k / \partial x\right|$. This is derived from FEA results and plotted in Figure 17. Note that there is a range of positions for each phase near the fully aligned and fully unaligned positions where the position sensitivity is low.

The flux/current scheme uses the active phases, and fortunately the commutation of the machine is such that the phases are excited during the period of maximum position sensitivity since, by Equation 2.1, the spatial rate of change of inductance is also related to the torque production of the machine. Thus, the design goal of maximizing torque per ampere is in congruence with the goal of maximizing position sensitivity.

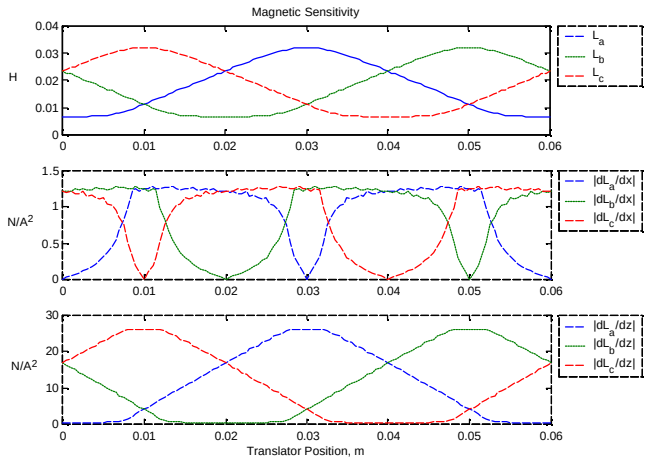

Figure 17. Inductance Profile, Position Sensitivity, and Air Gap Sensitivity

Note the good overlap between the regions of high position sensitivity. This is the same phenomenon that makes ripple-free torque production possible using multiphase excitation. With multiphase excitation, there is always at least one phase of the machine being excited and there is a smooth transition between the phases. During this excitation period, the flux linkage builds to a point where it can be used for accurate position sensing. This is fortunate for the flux/current sensorless technique because it means that the position estimate can be accomplished continuously with good accuracy, provided an optimal phase selection algorithm that is able to switch from one phase to another at the appropriate time. Again, the design goals of ripple free force production and accurate sensorless positioning are in congruence.

4.3.3.5 Air Gap Variations

Perhaps the most significant source of error in the prototype linear switched reluctance configuration stems from the fact that the FEA results are all computed with the assumption of a fixed air gap between translator and stator. While rotary switched reluctance motors benefit from stiff rotating bearings to

insure minimal air gap fluctuations, the prototype linear switched reluctance system is afforded no such mechanical regularities. The control system for a linear switched reluctance motor finds itself in the very shaky rolling world of gravity and steel wheels rolling on roughshod sledge-hammer steel I-beams. The translator is attached to a vehicle that rolls on steel wheels and the stator is mounted to a steel I-beam. For the linear SRM, vibration of the traveling vehicle causes air gap variations which are orders of magnitude more significant than in rotary SRMs. This linear machine has the loose construction of a rolling carriage and more degrees of freedom than the rotating SRM. Due to mechanical imperfections, the distance between the translator and stator vary while the vehicle is in motion. The exact amount of uncertainty resulting from the air gap fluctuation is difficult to quantify in a single term due to the mechanical imperfection itself, but the calculation below should give a rough estimate. As a very conservative estimate, let's assume that the fluctuation relative to the nominal air gap, Δz, is equal to 20 percent of the nominal gap or 200 μm. Since the mean magnetic sensitivity of the inductance to air gap variations during excitation is about 15 N/A^2, we expect the flux linkage uncertainty to be as follows.

$$dl_{gap} = \Delta z \cdot \frac{\partial L_k}{\partial z} \cdot \bar{i} = 200 \times 10^{-6} \cdot 15 \cdot 2.45 = 7.35 \times 10^{-3}\ \mathrm{V \cdot s} \tag{4.48}$$

Significantly, the flux linkage uncertainty from only a 200 μm air gap fluctuation is roughly 95 times greater than the total random flux linkage uncertainty (77.6 μV·s). Thus, referencing Figure 17, the inductive air gap sensitivity is roughly twenty times greater than the position sensitivity. In addition, the air gap sensitivity varies over the range of travel and is greatest at the aligned position. This implies that air gap variations are perhaps the most important source of error and may significantly influence the performance of the

position estimation system. In effect, the LSRM position sensing system is roughly 20 times more sensitive to vertical air gap travel than linear travel. This characteristic implies that the effects of air gap fluctuations must be considered in the design of LSRMs, and that it may be desirable to mitigate air gap fluctuations if position sensorless control is desired.

4.3.3.6 Time Delay

This source of error is related to the frequency at which sensorless position estimates are updated by the add-on system. Although the implementation provides data acquisition at a sampling rate of 10,000 Samples/Second, position updates are provided at only about 77 Updates/Second due to computational speed limitations. The signals are acquired continuously, stored in a FIFO memory buffer, and then read from the FIFO roughly 130 samples at a time and processed to yield one position estimate. Thus, each position estimate is computed using data that is about 13 milliseconds old. This is problematic if the vehicle is moving, since the estimated position will lag behind the true position significantly. This introduces a phase lag that could prevent operation or even cause instability in the control loop. The amount of error caused by this phase delay depends on the vehicle velocity and can be approximated as follows.

$$dx_{lp} \approx \frac{vel}{f_{lp}} = \frac{vel}{76.9} \text{ m} \tag{4.49}$$

This error is plotted versus velocity in Figure 18, showing that it is a significant source of error that reaches 10 mm in magnitude at a velocity of 0.77 m/s, or roughly half the rated velocity of the machine. Since the LSRM is commutated on roughly 10 mm intervals, this source of delay and position error certainly must be reduced for successful closed-loop operation. This could be accomplished through the use of a faster algorithm or processor.

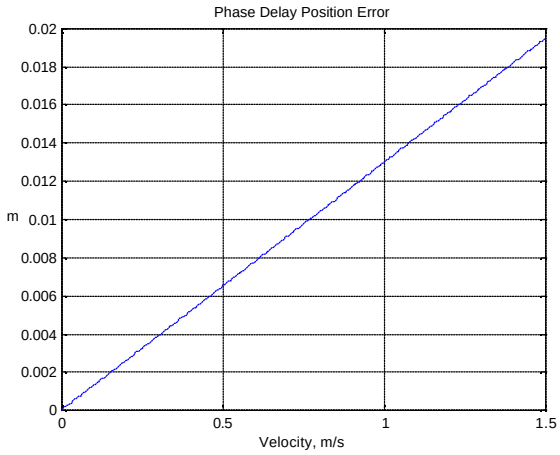

Figure 18. Expected Position Error Due to Phase Delay

4.4 Operational Results

Although successful closed-loop operation of the LSRM prototype using the sensorless position estimate was not achieved, it is hoped that a great deal of useful insight may nonetheless be obtained from this study. In this section, the position estimation scheme is evaluated experimentally by comparison to a mechanical position sensor with a resolution of 10 micrometers.

The error of the flux linkage calculation is evaluated by comparing the flux linkage value calculated by the estimator with that expected from FEA results. This is accomplished by loading the flux linkage and current FEA data into a LUT indexed by position and current. Position information from the mechanical position encoder is used to provide the position and measured current is used for the other input. This diagnostic exercise has error of its own but it is hoped that a rough gauge of the estimation algorithm might nonetheless be obtained through this approach.

Experimental results during a time period that includes a change of direction are plotted in Figure 19. It can be seen that the flux linkage diverges from the FEA value significantly, and diverges the most when the change in direction occurs and the vehicle velocity is minimum. From the error analysis, we expect the flux linkage integration drift to be most pronounced at low speeds. The results also indicate significant error in the estimated relative position, and the amount of error is greatest at low speeds. The optimal phase selection algorithm can also be observed.

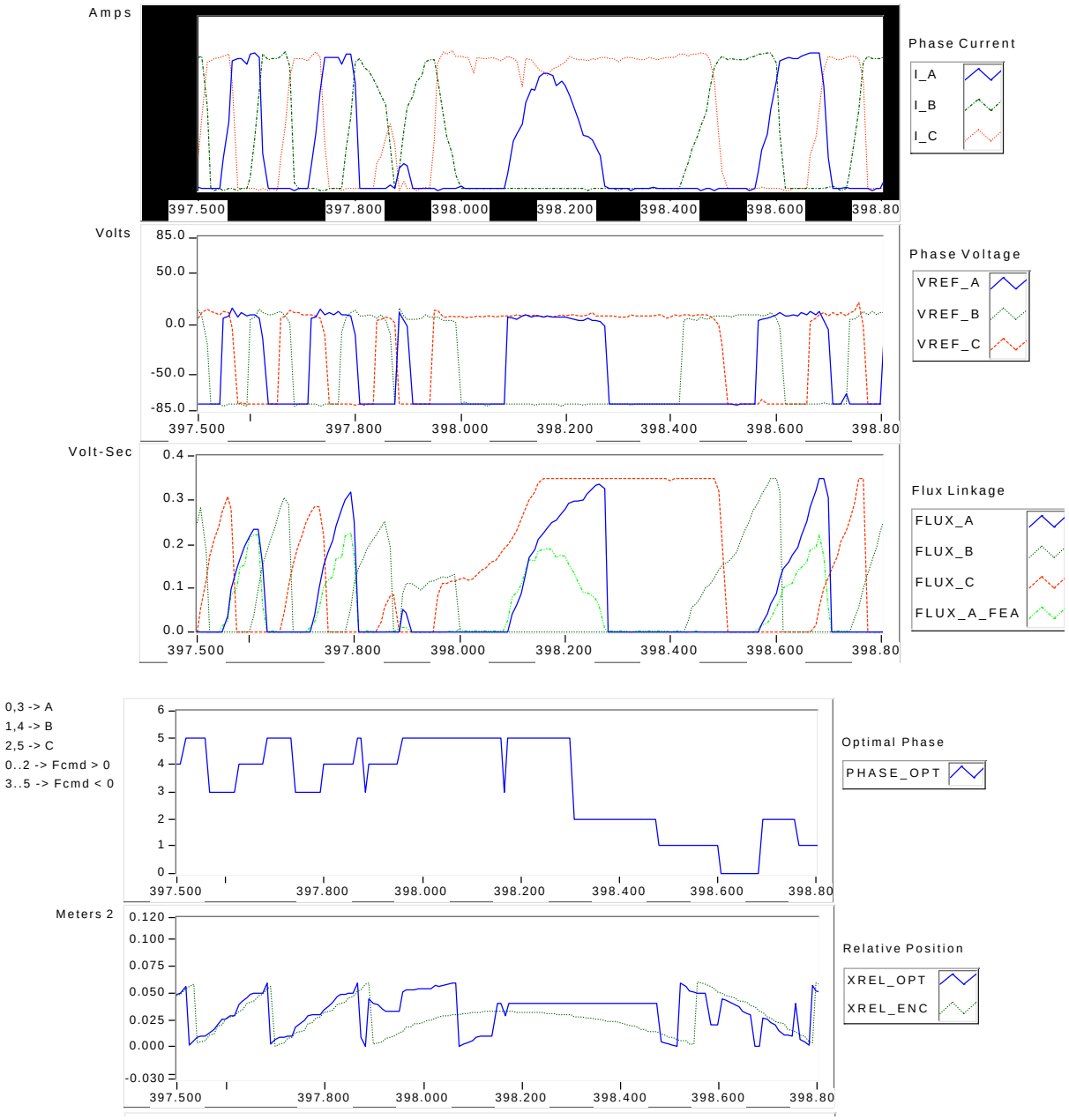

Figure 19. Comparison of Flux Linkage and Relative Position to Expected Values

Chapter 5

SUMMARY

5.1 Major Results

Linear Switched Reluctance Machines (LSRMs) are linear actuators suitable for a wide array of applications due to their energy efficiency and low cost. An important criticism of LSRMs, however, is that they require accurate position information for high performance control. In recent studies at Virginia Tech, a novel LSRM prototype has been developed along with a machine design procedure and a high performance unipolar switching converter and low force ripple control design [2, 3]. This study investigates the use of a sensorless positioning algorithm to eliminate the quadrature encoder position sensor assembly and related hardware. In sensorless positioning schemes, the position dependence of a magnetic property is used to determine the location of the translator/rotor for precise commutation by the control system.

This study begins with a description of the 4.8 m prototype LSRM machine design, converter and control system. The prototype was developed in the Spring of 1998 as a research test bed and proof-of-concept model in a joint effort between the Virginia Tech Motion Control Systems Research Group and the student-run Personal Electric Rapid Transit Systems division of the Virginia Tech Virtual Corporation, under the direction of Dr. Krishnan Ramu. The prototype features a unipolar switching topology to achieve accurate current control, a force distribution scheme for minimal force ripple, and cascaded control loops for force, velocity and position control. In the context of the sensorless positioning algorithm, the most important operational characteristics of the DSP control

system are presented. Two simulation models assist in the development of a sensorless positioning algorithm and are used to model the behavior of the existing vehicle dynamics, commutation scheme, and control system. The first model focuses on the Newtonian vehicle motional dynamics. The second simulation model concentrates on the machine equations, power electronics, unipolar switching converter topology, and the variable inductance phase winding dynamics.

The goal in this investigation is the development of a novel add-on sensorless position estimation system for a Linear Switched Reluctance Machine (LSRM). Unlike most of the existing sensorless algorithms proposed in literature, the objective is to add sensorless capabilities to the existing (position-sensor based) system with little or no modifications to the existing machine design, converter, and control system. The proposed position estimator is a "retrofit" solution with the goal of achieving sensorless operation with minimal modifications to the existing prototype and its high-performance control characteristics. In this approach, the position transducer is removed and replaced by a data acquisition system and processor that form the sensorless position estimation system. The inputs to the estimator are the phase voltages and currents in the converter, while the output is a position signal in quadrature encoder format designed to emulate the existing position sensor. This "retrofit" approach presents an interesting design challenge and places significant restrictions on the sensorless estimator design.

A flux/current method utilizing the voltage and current in an active phase is chosen for the LSRM implementation, since no signal injection is required and the active phase windings can be used without disturbing operation. Finite Element Analysis (FEA) is used to characterize the position dependence of the flux linkage over half of the translator cycle, and produce a look-up table that

maps flux linkage and current back to relative position. During operation, the current is measured directly from the phases and the flux linkage is calculated via integration of the phase voltage command and phase current. The phase voltage command is used to approximate the true phase voltage. Direct measurement of the phase voltage was deemed impractical since one sensor per phase winding would be required. The flux linkage calculation is mapped to relative translator position via a two-dimensional look-up table. Then an algorithm is used to convert from relative position to absolute position. Finally the absolute position is converted to a quadrature encoder signal and cabled to the DSP for use in the control system.

In Chapter 3, a survey of existing sensorless positioning algorithms is presented and used as a context for the selection of an algorithm for the prototype linear machine. The approaches described in literature almost always apply to rotary Switched Reluctance Machines, and little research exists about sensorless applications in linear machines. Some of the similarities and differences between linear and rotary sensorless algorithms with respect to cost, accuracy, and implementation are explored. A flux/current method is proposed for the prototype LSRM and its key features and components are described. The flux/current approach, also called the self-voltage technique, is chosen because no special test pulses are required and only the active phases are used. This makes possible the implementation of a retrofit sensorless positioning solution that preserves the normal operation of the converter and control system.

The flux/current approach is implemented in hardware and software and tested both independently of the control system (open loop) and in place of the position sensor (closed loop). Although successful operation of the prototype using the sensorless system is not achieved, the system provides an excellent test bed and yields valuable engineering design results. Through in depth study, it is

found that several important factors have prevented successful operation of the prototype using the sensorless estimator. Physical error sources such as air gap fluctuations and limitations in the computational speed of the estimator are found to be very significant.

Statistical techniques are used to analyze the sources and propagation of error in the estimator using a combination of analytical and experimental values. The total uncertainty in the flux linkage calculation is computed, and then used to find the total uncertainty in the sensorless position estimate. It is found that the predominant sources of error are systematic rather than random in nature. Unlike a rotary machine, the distance between the translator and stator in the prototype is susceptible to large variations because the prototype rolls on wheels. Through analysis of the prototype machine topology via Finite Element Analysis, it is found that the flux linkage is roughly twenty times more sensitive to variations in air gap than to variations in position.

Another large error source stems from the delays involved in the sensorless computation algorithm running on the real-time processing system. Due to insufficient processing power for the DSP task, the estimation processing system effectively introduces phase delay and additional position uncertainty of about 5 mm at an operational speed of 0.4 m/s. Significantly higher loop rates are required for an adequately performing sensorless positioning system. An additional algorithmic problem is that the uncertainty of the absolute position estimate increases over time due to integrator drift and the nature of the conversion process between relative and absolute position.

5.2 Recommendations for Future Study

Since one of the most predominant sources of error appears to be the result of air gap variations, it may be necessary to take corrective actions that involve

hardware changes. Air gap fluctuations could be reduced by improved mechanical construction of the track and vehicle, or an air gap sensor could be added so that variations could be accounted for in the algorithm. In the case of a LSRM used in a magnetic levitation system, air gap information may be readily available and might be used as an input to the position Look Up table.

The next most important source of error appears to stem from the loop time of the position estimation algorithm, which introduces phase delay and speed-dependent position error. Using a faster processor for the sensorless algorithm would solve this problem.

These problems also indicate some of the weaknesses of a "retrofit" approach to sensorless positioning. Most traditional sensorless positioning schemes utilize inactive phases to obtain the position estimate by applying a test signal. This requires significant modifications to the position sensor based control design but is well documented in many successful implementations.

One problem that might be addressed in future research is the conversion between relative and absolute position. An alternative algorithm that yields absolute position without drift might be feasible. The fixed location of the phase windings on the stator can be used a reference for computation of the absolute vehicle location from a Look Up table. Detailed discussion of this topic is outside the scope of this document.

Starting and low-speed characteristics should also be examined in greater detail for the LSRM, since the proposed scheme suffers from poor convergence of the flux linkage integral at low speed. It may be desirable to implement a different sensing approach at low speed, such as a discrete current rise/fall time method using inactive phases.

It is hoped that this thesis will provide a useful case study with many useful and interesting results for engineers involved in the development of sensorless control systems for Linear Switched Reluctance Machines. The author will be satisfied if he has done just a little something to advance the evolution of the perfect motor of the future. May the cultivation of technology bring prosperity, peace and nourishment for all living things and impart a wisdom that encourages a respectful and wondrous integration of human and Universe.

REFERENCES

[1] R. Krishnan, *Sensorless Operation of SRM Drives*, Lecture Notes, Bradley Department of Electrical Engineering, Virginia Polytechnic Institute and State University, 2000.

[2] B. S. Lee, H. K. Bae, P. Vijayraghavan, and R. Krishnan, "Design of a Linear Switched Reluctance Machine," in *IEEE Trans. on Ind. App.*, Nov./Dec. 2000.

[3] H. K. Bae, B. S. Lee, P. Vijayraghavan, and R. Krishnan, "A Linear Switched Reluctance Motor: Converter and Control," in *IEEE Trans. on Ind. App.*, Sept./Oct. 2000.

[4] H. K. Bae, "Control of Switched Reluctance Motors Considering Mutual Inductance," in *Virginia Tech P.h.D. Dissertation*, Blacksburg, VA, Aug. 2000.

[5] H. K. Bae and R. Krishnan, "A Novel Approach To Control of Switched Reluctance Motors Considering Mutual Inductance," in *IEEE Ind. Elect. Society Ann. Mtg.*, Conf. Rec., Oct. 2000.

[6] H. K. Bae, and R. Krishnan, "A Study of Current Controllers and Development of a Novel Current Controller for High Performance SRM Drives," in *IEEE Ind. App. Society Ann. Mtg.*, pp. 68-75, 1996.

[7] M. G. Jovanovic, R. E. Betz, and D. Platt, "Sensorless Vector Controller for a Synchronous Reluctance Motor," in *IEEE Trans. On Ind. App.*, vol. 34, no. 2, Mar./Apr. 1998.

[8] J. Hirai, T. W. Kim, and A. Kawamura, "Position-Sensorless Drive of Linear Pulse Motor for Suppressing Transient Vibration," in *IEEE Trans. On Ind. Elect.*, vol. 47, no. 2, Apr. 2000.

[9] A. D. Cheok, and N. Ertugrul, "Use of Fuzzy Logic for Modeling, Estimation, and Prediction Switched Reluctance Motor Drives," in *IEEE Trans. On Ind. Elect.*, vol. 46, no. 6, Dec. 1999.

[10] A. D. Cheok, and N. Ertugrul, "High Robustness of an SR Motor Angle Estimation Algorithm Using Fuzzy Predictive Filters and Heuristic Knowledge-Based Rules," in *IEEE Trans. On Ind. Elect.*, vol. 46, no. 5, Oct. 1999.

[11] D. S. Reay, and B. W. Williams, "Sensorless Position Detection using Neural Networks for the Control of Switched Reluctance Motors," in *Proc. of the 1999 IEEE*

Intl. Conf. on Control App., Aug. 1999.

[12] P. Laurent, M. Gabsi, and M. Multon, "Sensorless Rotor Position Analysis using Resonant Method For Switched Reluctance Motor," in *Proc. of the IEEE Ind. App. Society Ann. Mtg.*, pp. 687–694, Oct. 1993.

[13] N. H. Mvungi, M. A. Lahoud, and J. M. Stephenson, "New Sensorless Position Detector for SR Drives," in *Conf. Rec. of the 4th Intl. Conf. on Power Elect. and Variable Speed Drives*, London, UK, Jul. 1990.

[14] W. F. Ray, and F. Erfan, "A Sensorless Method for Determining Rotor Position for Switched Reluctance Motors," in *Conf. Rec. of the Intl. Conf. on Power Elect. and Variable Speed Drives*, London, UK, Oct. 1994.

[15] A. Broesse, and G. Henneberger, "Sensorless control of a switched reluctance motor using a Kalman filter," in *Conf. Rec. of the 7th Intl. Conf. on Power Elect. and Variable Speed Drives*, London, UK, Sept. 1998.

[16] H. S. Ooi, and T. C. Green, "Simulation of Neural Networks to Sensorless Control of Switched Reluctance Motor," in *Conf. Rec. of the 7th Intl. Conf. on Power Elect. and Variable Speed Drives*, London, UK, Sept. 1998.

[17] P. Jinupun, and P. C. K. Luk, "Direct Torque Control for Sensor-Less Switched Reluctance Motor Drives," in *Conf. Rec. of the 7th Intl. Conf. on Power Elect. and Variable Speed Drives*, London, UK, Sept. 1998.

[18] M. Ehsani, and K. R. Ramani, "New Commutation Methods Switched Reluctance Motors Based on Active Phase Vectors," in *Proc. of the 25th Ann. IEEE Power Elect. Specialists Conf.*, Taipei, 1994.

[19] M. Ehsani, I. Husain, and A. B. Kulkarni, "Elimination of Discrete Position Sensor and Current Sensor Switched Reluctance Motor Drives," in *IEEE Trans. on Ind. App.*, vol. 28, no. 1, Jan./Feb. 1992.

[20] G. Gallegos-Lopez, P. C. Kjaer, and T. Miller, "A New Sensorless Method for Switched Reluctance Motor Drives," in *IEEE Trans. on Ind. App.*, vol. 34, no. 4, Jul./Aug. 1998.

[21] S. K. Panda, and G. A. J. Amaratunga, "Switched Reluctance Motor Drive Without Direct Rotor Position Sensing," in *Conf. Rec. of the IEEE Ind. App. Society Ann. Mtg.*, Seattle, Oct. 1990.

[22] U. S. Deshpande, J. J. Cathey, and E. Richter, "A High Force Density Linear Switched

Reluctance Machine," in *Conf. Rec. of the IEEE Ind. App. Society Ann. Mtg.*, vol. 1, Toronto, Oct. 1993.

[23] I. Boldea and S. A. Nasar, *Linear Electric Actuators and Generators*, Cambridge University Press, UK, 1997.

[24] P. Kaurent, M. Gabsi, and B. Multon, "Sensorless Rotor Position Analysis Using Resonant Method for Switched Reluctance Motor," in *Conf. Rec. of the IEEE Ind. App. Society Ann. Mtg.*, Toronto, Canada, Oct. 1993.

[25] A. Cheok, and N. Ertugal, "A Model Free Fuzzy Logic Based Rotor Position Sensorless Switched Reluctance Motor Drive," in *Conf. Rec. of the 1996 IEEE Ind. App. Society Ann. Mtg.*, San Diego, CA, Oct. 1996.

[26] P. Pillay, Y. Liu, W. Cai, and T. Sebastian, "Multiphase Operation of Switched Reluctance Motor Drives," in *Conf. Rec. of the 1997 IEEE Ind. App. Society Ann. Mtg.*, vol. 1, New Orleans, LA, Oct. 1997.

[27] M. T. DiRenzo, and W. Khan, "Self-Trained Commutation Algorithm for an SR Motor Drive System without Position Sensing," in *Conf. Rec. of the 1997 IEEE Ind. App. Society Ann. Mtg.*, vol. 1, New Orleans, LA, Oct. 1997.

[28] L. Xu, and J. Bu, "Position Transducerless Control of a Switched Reluctance Motor Using Minimum Magnetizing Input," in *Conf. Rec. of the 1997 IEEE Ind. App. Society Ann. Mtg.*, vol. 1, New Orleans, LA, Oct. 1997.

[29] A. Cheok, and N. Ertugal, "Use of Fuzzy Logic for Modeling, Estimation, and Prediction Switched Reluctance Motor Drives," in *IEEE Trans. on Ind. App.*, vol. 46, no. 6, Dec. 1999.

[30] E. Mese, and D. A. Torrey, "Sensorless Position Estimation for Variable Reluctance Machines Using Artificial Neural Networks," in *Conf. Rec. of the 1997 IEEE Ind. App. Society Ann. Mtg.*, vol. 1, New Orleans, LA, Oct. 1997.

[31] A.V. Rajarathnam, B. Fahimi, and M. Ehsani, "Neural Network Based Self-Tuning Control of a Switched Reluctance Motor Drive to Maximize Torque per Ampere," in *Conf. Rec. of the 1997 IEEE Ind. App. Society Ann. Mtg.*, vol. 1, New Orleans, LA, Oct. 1997.

[32] G. Suresh, K.M. Rahman, B. Fahimi, and M. Ehsani, "Self-tuning Sensorless SRM Drives for Low Cost Mass Production," in *Conf. Rec. of the 1998 IEEE Ind. App. Society Ann. Mtg.*, vol. 1, Saint Louis, MO, Oct. 1998.

[33] J. Bu, and L. Xu, "Eliminating Starting Hesitation for Reliable Sensorless Control of Switched Reluctance Motors," in *Conf. Rec. of the 1998 IEEE Ind. App. Society Ann. Mtg.*, vol. 1, Saint Louis, MO, Oct. 1998.

[34] A. Bellini, F. Filippetti, G. Franceschini, C. Tassoni, and P. Vas, "Position Sensorless Control of a SRM Drive Using ANN-Techniques," in *Conf. Rec. of the 1998 IEEE Ind. App. Society Ann. Mtg.*, vol. 1, Saint Louis, MO, Oct. 1998.

[35] N.J. Nagel, R.D. Lorenz, "Rotating Vector Methods for Sensorless, Smooth Torque Control of a Switched Reluctance Motor Drive," in *Conf. Rec. of the 1998 IEEE Ind. App. Society Ann. Mtg.*, vol. 1, Saint Louis, MO, Oct. 1998.

[36] G. Gallegos-Lopez, P. C. Kjaer, T. J. E. Miller, "High-grade Position Estimation for SRM Drives Using Flux Linkage/Current Correction Model," in *Conf. Rec. of the 1998 IEEE Ind. App. Society Ann. Mtg.*, vol. 1, Saint Louis, MO, Oct. 1998.

[37] B. Y. Ma, W. S. Feng, T. H. Liu, and C. G. Chen, "Design and Implementation of a Sensorless Switched Reluctance Drive System," in *IEEE Trans. on Aerospace and Electronic Systems*, vol. 34, no. 4, Oct. 1998.

[38] J. T. Bass, M. Ehsani, T. J. E. Miller, "Robust Torque Control of Switched Reluctance Motors Without a Shaft Position Sensor," in *IEEE Trans. on Ind. Elect.*. vol. IE-33, no. 3, pp. 212-216, Aug. 1986.

[39] D. S. Reay, Y. Dessouky, and B.W. Williams, "The Use of Neural Networks to Enhance Sensorless Position Detection Switched Reluctance Motors," in *Proc. of the IEEE Intl. Conf. on Systems, Man and Cybernetics*, Piscataway, NJ, vol. 2, pp. 1774-1778, 1998.

[40] G. Suresh, B. Fahimi, M. Ehsani, "Improvement of the Accuracy and Speed Range Sensorless Control of Switched Reluctance Motors," in *Conf. Rec. of the 13th Ann. Applied Power Elect. Conf. and Exposition*, Anaheim, CA, vol. 2, Feb. 1998.

[41] S. Vukosavic, L. Peric, E. Levi, and V. Vuckovic, "Sensorless Operation of the SR Motor with Constant Dwell Angle," in *Conf. Rec. of the 21st Ann. IEEE Power Elect. Specialists Conf.*, vol. 1, San Antonio, TX, 1990.

[42] M. Ehsani, and K. R. Ramani, "Direct Control Strategies Based on Sensing Inductance Switched Reluctance Motors," in *Conf. Rec.*

of the 24th Ann. IEEE Power Elect. Specialists Conf., 1993.

[43] M. Ehsani, S. Mahajan, K. R. Ramani, and I. Husain, "New Modulation Encoding Techniques for Indirect Rotor Position Sensing Switched Reluctance Motors," in *IEEE Transactions on Industry Applications*, College Station, TX, vol. 30, pp. 85 – 91, Jan./Feb. 1994.

[44] S. K. Panda, and G. Amaratunga, "Comparison of Two Techniques for Closed-Loop Drive of VR Step Motors Without Direct Rotor Position Sensing," in *IEEE Trans. on Ind. Elect.*, vol. 38, no. 2, pp. 95-101, Apr. 1991.

[45] P. P. Acarnley, R. J. Hill, and C. W. Hooper, "Detection of Rotor Position Stepping and Switched Motors by Monitoring of Current Waveforms," in *IEEE Trans. on Ind. Elect.*, vol. IE-32, no. 3, pp. 215-222, Aug. 1985.

[46] S. K. Panda, and G. A. J. Amaratunga, "Waveform Detection Technique for Indirect Rotor-Position Sensing of Switched Reluctance Motor Drives," in *IEE Proc. on Elect, Power App.*, Singapore, vol. 140, no. 1, pp. 89-96, Jan. 1993.

[47] S. P. Liou, and W. Wang, "Indirect Rotor Position Sensing for Switched Reluctance Motor Using Search Coil," in *Proc. of the 1996 Canadian Conf. on Elect. and Comp. Eng.*, San Francisco, CA, vol. 2, pp. 939-942, May 1996.

[48] R. Krishnan, and P. Materu, "Measurement and Instrumentation of a Switched Reluctance Motor," in *Proc. of the 1989 Ind. App. Society Ann. Mtg.*, San Diego, CA, Oct. 1989.

[49] T. Perl, I. Husain, and M. Elbuluk, "Design Trends and Trade-offs for Sensorless Operation of Switched Reluctance Motor Drives," in *Proc. of the Thirtieth IAS Ann. Mtg.*, Akron, OH, vol. 1, pp. 278-285, Oct. 1995.

[50] J. P. Lyons, S. R. MacMinn, and M. A. Preston, "Flux/Current Methods for SRM Rotor Position Estimation," in *Conf. Rec. of the Ind. App. Society Ann. Mtg.*, Dearborn, MI, 1991, pp. 482-487.

[51] M. Ehsani, I. Husain, and K. R. Ramani, "An Analysis of the Error Indirect Rotor Position Sensing of Switched Reluctance Motors," in *Conf. Rec. of the 1991 IEEE IECON*, Oct. 1991.

[52] S. R. Macminn, P. M. Szczesny, W. J. Rzesos, and T. M. Jahns, "Application of Sensor Integration Techniques to Switched Reluctance Motor Drives," in *Conf. Rec. of the 1988 IEEE Ind. App. Society Ann. Mtg.*, pp. 584-588, Oct. 1998.

[53] A. Kawamura, "Survey of Position Sensorless Switched Reluctance Motor Control," in *Conf. Rec. of the 1994 IEEE IECON*, pp. 1595-1598, 1994.

[54] W. F. Ray, and I. H. Al-Bahadly, "Sensorless Methods for Determining the Rotor Position of Switched Reluctance Motors," in *Fifth European Conf. on Power Elect. and App.*, Nottingham, UK, vol. 6, pp. 7-13, 1993.

[55] A. Lumsdaine, J. H. Lang, and M. J. Bales, "A State Observer for Variable Reluctance Motors," in *Nineteeth Asilomar Conf. on Circuits, Systems and Comp.*, pp. 660-664, Nov. 1985.

[56] M. Ehsani, and I. Husain, "Rotor Position Sensing in Switched Reluctance Motor Drives by Measuring the Mutually Induced Voltages," in *IEEE Trans. on Ind. App.*, vol. 30, no. 3, May/Jun. 1994.

[57] K. Beauchamp, and C. Yuen, *Data Acquisition for Signal Analysis*, George Allen & Unwin, London, UK, pp. 117-118, 1980.

[58] J. R. Taylor, "An Introduction to Error Analysis: The Study of Uncertainty Physical Measurements," University Science Books, Mill Valley, CA, 1982.

[59] R. M. Crowder, *Electric Drives and their Controls*, Clarendon Press, Oxford, pp. 55-81, 1995.

[60] N. M. Mvungi, M. A. Lahoud, and J. M. Stephenson, "A New Sensorless Position Detector for SR Drives," in *Fourth Intl. Conf. on Power Elect. and Variable-Speed Drives*, pp. 249-252, 1990.

[61] F. Kirchhoff, and R. Hanitsch, "A Sensorless SRM Drive without A/D and D/A Converters," in the Proc. of the Intl. Conf. on Elect. Machines, v. 613, pp. 314-317, 1994.

[62] W. D. Harris, and J. D. Lang, "Simple Motion Estimator for VR Motors," in *Proc. of the 1998 IEEE Ind. App. Society Mtg.*, 1998.

[63] B. Y. Ma, T. H. Liu, T. J. Shen, and W. S. Feng, "Design and Implementation of a Sensorless Switched Reluctance Motor Drive System," in *IEEE Trans. on Aerospace and Elect. Systems*, vol. 34, no. 4, pp. 1193-1207, Oct. 1998.

[64] V. K. Sharma, B. Singh, and S. S. Murthy, "A Frequency Response Method to Estimate Inductance Profile of a Switched Reluctance Motor," in *Proc. of the 1997 Intl. Conf. on Power Elect. and Drive Systems.*, vol. 1, pp. 181 -187, 1997